AGU ADVANCING EARTH AND SPACE SCIENCES

Earth and Space Science

RESEARCH ARTICLE
10.1029/2025EA004379

Robust Edge Detection for Structural Mapping Beneath the Aristarchus Plateau on the Moon Using Gravity Data

Hanbing Ai[1], Qian Huang[1,2], Yunus Levent Ekinci[3,4], Ahmad Alvandi[5], and Satya Narayan[6]

[1]Hubei Subsurface Multi-Scale Imaging Key Laboratory, School of Geophysics and Geomatics, China University of Geosciences, Wuhan, China, [2]Hubei Key Laboratory of Planetary Geology and Deep-Space Exploration, School of Earth Sciences, China University of Geosciences, Wuhan, China, [3]Department of Art History, Bitlis Eren University, Bitlis, Türkiye, [4]Faculty of Applied Sciences, Muş Alparslan University, Muş, Türkiye, [5]Institute of Geophysics, University of Tehran, Tehran, Iran, [6]Oil and Natural Gas Corporation Limited, Dehradun, India

Key Points:

- This paper combines edge enhancement, fast imaging, and inversion methods to achieve reliable results from lunar gravity anomalies
- Several noise reduction techniques are investigated and compared to improve edge-detection performance
- The findings support the low-density zone beneath the Aristarchus crater

Correspondence to:
Q. Huang,
qianhuang@cug.edu.cn

Citation:
Ai, H., Huang, Q., Ekinci, Y. L., Alvandi, A., & Narayan, S. (2025). Robust edge detection for structural mapping beneath the Aristarchus Plateau on the Moon using gravity data. *Earth and Space Science*, *12*, e2025EA004379. https://doi.org/10.1029/2025EA004379

Received 29 MAR 2025
Accepted 29 JUL 2025

Author Contributions:
Conceptualization: Hanbing Ai, Qian Huang, Yunus Levent Ekinci, Ahmad Alvandi, Satya Narayan
Data curation: Hanbing Ai, Qian Huang, Yunus Levent Ekinci, Ahmad Alvandi
Formal analysis: Hanbing Ai, Qian Huang, Yunus Levent Ekinci
Funding acquisition: Qian Huang
Investigation: Hanbing Ai, Qian Huang, Yunus Levent Ekinci, Ahmad Alvandi
Methodology: Hanbing Ai, Qian Huang, Yunus Levent Ekinci, Ahmad Alvandi
Project administration: Hanbing Ai, Qian Huang
Resources: Hanbing Ai, Qian Huang, Yunus Levent Ekinci, Satya Narayan
Software: Hanbing Ai, Qian Huang, Satya Narayan
Supervision: Hanbing Ai
Validation: Hanbing Ai, Qian Huang, Yunus Levent Ekinci, Ahmad Alvandi, Satya Narayan
Visualization: Hanbing Ai, Qian Huang, Yunus Levent Ekinci, Ahmad Alvandi, Satya Narayan

Abstract Accurately detecting the edges of subsurface geological structures from potential field anomalies remains a fundamental challenge. We applied the HTHG (Hyperbolic tangent function with horizontal and vertical derivatives of Total Horizontal Derivative) method to enhance subtle details in lunar gravity anomalies, focusing on the Aristarchus region and its surroundings. Initial assessments were conducted on synthetic noise-free and noisy gravity data sets and compared against eleven representative edge detectors. In the noise-free data case, HTHG demonstrated superior performance over other detectors in terms of accuracy, resolution, sharpness, and amplitude balancing. However, similar to other approaches, its directional derivative calculations are highly susceptible to noise amplification. To address this challenge, we implemented various noise reduction techniques, including the β-VDR and MNLM methods. Notably, we also presented different methods for estimating the tuning parameters of the involved noise attenuation methods. HTHG, in conjunction with MNLM, demonstrated the most superior performance. We subsequently applied the HTHG operator to lunar gravity anomalies from the Aristarchus region. Our results were compared with the outputs of 2D inversion employing a mixed-weighted function, a correlation imaging algorithm, and 3D inversion enhanced by spectral analysis. Our findings indicate that the Aristarchus crater hosts a low-density subsurface mass. The outcomes of this study confirm the robust performance of the HTHG method in addressing edge detection challenges and underscore the necessity of integrating various methods, including edge detection, noise suppression, fast imaging, and inversion, to guarantee the interpretation reliability and advance our understanding about the internal architecture of the Moon.

1. Introduction

The Gravity Recovery and Interior Laboratory (GRAIL) mission yielded high-resolution lunar gravity anomalies that are indispensable for investigating the Moon's internal structure (Goossens et al., 2020; Konopliv et al., 2014; Yin et al., 2024; Zuber et al., 2013). Building upon these high-resolution data sets, earlier studies have concentrated on distinct lunar regions, specifically volcanic regions marked by high-density intrusions (Huang et al., 2020; Kiefer, 2013). In addition, studies have extended to large impact basins, where observed mass concentrations are associated with mantle upwelling and the consequent thinning of the lunar crust (Liang et al., 2014; Zhao et al., 2021). The Aristarchus plateau is of considerable scientific interest, evidenced by its abundant volcanic features. These characteristics point to the presence of underlying structures, such as magma chambers or intrusions, which may have played a role in sustaining previous volcanic processes. The Aristarchus Plateau is a prominent, four-sided raised landform situated on the northwestern near side of the Moon. This geologically complex plateau, approximately 170 km × 220 km in extent and rising 2 km above the younger neighboring basaltic plains, encompasses notable volcanic and impact features, including the Aristarchus and Herodotus craters, along with Vallis Schröteri which is the largest sinuous rille on the natural satellite. It is bounded by vast lava flows and overlain by one of the Moon's most extensive regional pyroclastic deposits, characterized by numerous silicic domes and exposed rock outcrops (Glotch et al., 2010; Zisk et al., 1977). Its complex geology and volcanic activity make the Aristarchus Plateau a high-priority target for future lunar landing missions and extended scientific exploration (Glotch et al., 2021). Given the distinctive geological characteristics of this plateau, extensive remote sensing studies have investigated its surface mineralogy using data from the Clementine UVVIS, NIR (Chevrel et al., 2009), and Chandrayaan-1's Moon Mineralogy Mapper device (Mustard

Writing – original draft: Hanbing Ai, Qian Huang, Yunus Levent Ekinci
Writing – review & editing: Hanbing Ai, Qian Huang, Yunus Levent Ekinci

et al., 2011). These researches discovered a basal anorthositic crust buried beneath extensive pyroclastic deposits. Subsurface models derived from gravity data can complement surface studies by offering deeper insights into the volcanic system of the plateau through the characterization of subsurface density variations. Lunar gravity field models, especially those derived from remote sensing data (e.g., Liang et al., 2014), offer a robust approach for delineating subsurface structures through the identification of high- and low-density zones. The GRGM1200L model, derived from the GRAIL mission (Goossens et al., 2020), which provides a 4.5 km resolution, is ideal for examining the subsurface nature of the Aristarchus Plateau. Comprehensive analyses of GRAIL data reveal that the crustal and load densities in the Aristarchus Plateau region average roughly 2,500 kg/m^3 (Huang et al., 2013). These results indicate the existence of igneous rocks that are critical for understanding the geological evolution of the region.

Edge-detection techniques applied to potential field data sets, such as gravity and magnetic, have emerged as powerful tools for delineating subsurface structures and are widely employed in geophysical investigations (e.g., Ai, Ekinci, et al., 2024, Ai, Deniz Toktay, et al., 2024; Al-Bahadily et al., 2024; Alvandi et al., 2024; Cooper and Cowan, 2006; Deniz Toktay et al., 2025; Ekinci and Yigitbas, 2015; Ekinci et al., 2013; Fedi and Florio, 2001; Ibraheem et al., 2023; Pham, 2023; Pham and Oliveira, 2023; Saibi et al., 2019; Ye et al., 2024). Numerous techniques have been developed to delineate causative source edges, each offering distinct advantages and inherent limitations. Challenges include vulnerability to artifacts, noise amplification during derivative calculations, limited spatial resolution, and difficulties in balancing amplitude responses from subsurface sources at varying depths (Liu et al., 2023). In this study, we utilized the recently proposed HTHG (Hyperbolic tangent function with horizontal and vertical derivatives of Total Horizontal Derivative) operator to robustly interpret lunar gravity anomalies acquired in the GRAIL task, thereby explaining subsurface structures within the Aristarchus region. Preliminary evaluations were conducted on synthetic gravity data sets comprising both noise-free and noisy cases to thoroughly compare the effectiveness of the HTHG operator against eleven well-established edge-detection techniques. We then investigated several noise reduction techniques with parameter tuning based on Lp norms and C norm to improve edge-detection performance. Finally, we applied the HTHG operator to lunar gravity anomalies from the Aristarchus region and validated the results by comparing them with 2D focusing inversion, the correlation imaging algorithm, and reported 3D inversion solutions integrated with spectral analysis. The outcomes of this study substantiated the effectiveness of the HTHG method in addressing edge detection challenges and underscore the necessity of integrating various methods, including edge detection, noise suppression, and inversion to guarantee the interpretation reliability and advance our understanding about the internal architecture of the Moon.

2. Methodology

The Total Horizontal DeRivative (THDR) operator, commonly utilized for delineating horizontal edges of anomaly sources using potential field data, was originally proposed by Cordell (1979). The THDR filter, given below, effectively maps shallow geological structures, exhibits reduced susceptibility to noise interference with first-order derivatives, and produces peak amplitudes aligned with geological boundaries (Cordell, 1979):

$$\mathrm{THDR} = \sqrt{\left(\frac{\partial f}{\partial x}\right)^2 + \left(\frac{\partial f}{\partial y}\right)^2} \tag{1}$$

where f is the input gravity anomaly, $\frac{\partial f}{\partial x}$ and $\frac{\partial f}{\partial y}$ are the first-order derivatives in horizontal directions. Nabighian (1984) later introduced the Analytic Signal Amplitude (ASA), which delineates the edges of buried sources by detecting ASA peak values. This filter is expressed by:

$$\mathrm{ASA} = \sqrt{\left(\frac{\partial f}{\partial x}\right)^2 + \left(\frac{\partial f}{\partial y}\right)^2 + \left(\frac{\partial f}{\partial z}\right)^2} \tag{2}$$

The ASA filter incorporates not only horizontal derivatives but also the first-order vertical derivatives of the potential field anomaly to enhance edge detection. However, both the THDR and ASA operators face challenges in balancing anomaly amplitudes from sources located at varying depths (Alvandi et al., 2023; Prasad et al., 2022). Consequently, a range of phase-based and normalized filters has been proposed to effectively

determine the edges of both shallow and deep-seated sources. The Tilt Angle (TA) filter, introduced by Miller and Singh (1994), normalizes the vertical derivatives using the THDR, and it is expressed by:

$$\mathrm{TA} = \tan^{-1}\left[\frac{\frac{\partial f}{\partial z}}{\mathrm{THDR}}\right] \tag{3}$$

The TA amplitude is positive over the source, zero at its boundaries, and negative beyond, varying within a range of ±90°. The Theta Map (TM) operator, proposed by Wijns et al. (2005), is a phase-based filter characterized by minimal amplitude at horizontal boundaries, with values ranging from 0 to 90°. The formulation of this filter is given by:

$$\mathrm{TM} = \cos^{-1}\left(\frac{\mathrm{THDR}}{\mathrm{ASA}}\right) \tag{4}$$

Verduzco et al. (2004) reported that the maximum amplitude of THDR of the TA (TA_THDR) provides a more detailed edge detection. TA_THDR is expressed by:

$$\mathrm{TA\_THDR} = \sqrt{\left(\frac{\partial TA}{\partial x}\right)^2 + \left(\frac{\partial TA}{\partial y}\right)^2} \tag{5}$$

TA_THDR illustrates amplitudes as positive over the sources and negative outside them. Later, Cooper and Cowan (2006) introduced the TDX filter, which produces maxima at source edges. This operator is defined as:

$$\mathrm{TDX} = \tan^{-1}\left[\frac{\sqrt{\left(\frac{\partial f}{\partial x}\right)^2 + \left(\frac{\partial f}{\partial y}\right)^2}}{\left|\frac{\partial f}{\partial z}\right|}\right] \tag{6}$$

Ferreira et al. (2013) proposed the TA of the THDR as follows:

$$\mathrm{TAHG} = \tan^{-1}\left(\frac{\mathrm{THDR}_z}{\sqrt{(\mathrm{THDR}_x)^2 + (\mathrm{THDR}_y)^2}}\right) \tag{7}$$

Ma et al. (2016) proposed the improved horizontal tilt angle (ITDX), which normalizes the THDR of the vertical derivatives by the second-order vertical derivatives as given in Equation 7. ITDX produces maxima over the source boundaries.

$$\mathrm{ITDX} = \tan^{-1}\left(\frac{\sqrt{\left(\frac{\partial^2 f}{\partial z \partial x}\right)^2 + \left(\frac{\partial^2 f}{\partial z \partial y}\right)^2}}{\left|\frac{\partial^2 f}{\partial z^2}\right|}\right) \tag{8}$$

Pham et al. (2019) proposed a dimensionless Logistic Total Horizontal Gradient (LTHG) function. Notably, the total horizontal gradient shares the same meaning of the THDR. By optimizing with a user-defined parameter α, LTHG effectively balances amplitudes and enhances the clarity of edge detection. The definition of this function is given below:

$$\mathrm{LTHG} = \left[1 + \exp\left(-\frac{\mathrm{THDR}_z}{\sqrt{(\mathrm{THDR}_x)^2 - (\mathrm{THDR}_y)^2}}\right)\right]^{-\alpha} \tag{9}$$

Basically, the parameter α, controlling the resolution of detected results, is determined via some trial-and-error experimentation. We will discuss its effect on the edge detection in next sections. Melouah and Pham (2021) introduced the Improved LTHG (ILTHG) by the expression given below:

$$\mathrm{ILTHG} = \left[1 + \exp\left(-\frac{\mathrm{ITHG}_z}{\sqrt{(\mathrm{ITHG}_x)^2 - (\mathrm{ITHG}_y)^2}}\right)\right]^{-\alpha} \tag{10}$$

where

$$\mathrm{ITHG} = \sqrt{\left(\frac{\partial^2 f}{\partial z \partial x}\right)^2 + \left(\frac{\partial^2 f}{\partial z \partial y}\right)^2} \tag{11}$$

This operator simultaneously balances the amplitudes of deep and shallow sources and provides maximum amplitudes over the source edges. The resolution of ILTHG is also controlled by the parameter α. Lately, Pham (2023) introduced MNTH, using ASA and the vertical derivative, as given below:

$$\mathrm{MNTH} = \tan^{-1}\left[\frac{ASA}{\left|\frac{\partial f}{\partial z}\right|}\right] \tag{12}$$

The MNTH peaks effectively delineate horizontal edges.

As described above, the arctangent function has been widely applied in boundary detection. However, it should be noted that the hyperbolic tangent function provides a slightly narrower dynamic range in its output [−1, 1] than the inverse tangent function [−π/2, π/2] (see Figure 1 in Ai, Ekinci, et al. (2024)). The main difference between the inverse tangent and hyperbolic tangent functions is that transitions occur more quickly with the latter. The hyperbolic tangent function effectively asymptotes to the maximum value, but the inverse tangent function asymptotes more slowly. Recognizing this slight difference, Ai, Ekinci, et al. (2024) introduced the HTHG (Hyperbolic tangent function with horizontal and vertical derivatives of Total Horizontal Derivative) detector. The HTHG formulation, expressed below, constrains boundary amplitudes within the range of −1 to +1.

$$\mathrm{HTHG} = \tanh\left[\frac{\mathrm{THDR}_z}{\sqrt{(\mathrm{THDR}_x)^2 + (\mathrm{THDR}_y)^2}} - \frac{\pi}{2}\right] \tag{13}$$

Peaks in the HTHG signal delineate source edges. A major advantage of the HTHG operator is its ability to sharply define the boundaries of anomalous bodies while effectively suppressing spurious edges. Moreover, unlike LTHG and ILTHG, the resolution of HTHG is inherently independent of user-defined parameters. Table 1 further gives a summary of the involved edge detection methods.

3. Synthetic Applications and Findings

The performance of 12 edge detection algorithms was analyzed using synthetic gravity data sets under both noise-free and noise-contaminated cases. The gravity response of a rectangular prismatic source is obtained by the spatial bounds of the source (Blakely, 1995; Plouff, 1976)

Table 1
Summary of the Edge Detection Methods Used in This Work

Edge detector used	Mathematical equation	Unit	Proposed by
THDR	$\sqrt{\left(\frac{\partial f}{\partial x}\right)^2 + \left(\frac{\partial f}{\partial y}\right)^2}$	mGal/km	Cordell (1979)
ASA	$\sqrt{\left(\frac{\partial f}{\partial x}\right)^2 + \left(\frac{\partial f}{\partial y}\right)^2 + \left(\frac{\partial f}{\partial z}\right)^2}$	mGal/km	Nabighian (1984)
TA	$\tan^{-1}\left[\frac{\frac{\partial f}{\partial z}}{\mathrm{THDR}}\right]$	Radian	Miller and Singh (1994)
TM	$\cos^{-1}\left(\frac{\mathrm{THDR}}{\mathrm{ASA}}\right)$	Radian	Wijns et al. (2005)
TA_THDR	$\sqrt{\left(\frac{\partial TA}{\partial x}\right)^2 + \left(\frac{\partial TA}{\partial y}\right)^2}$	Radian/km	Verduzco et al. (2004)
TDX	$\tan^{-1}\left[\frac{\sqrt{\left(\frac{\partial f}{\partial x}\right)^2 + \left(\frac{\partial f}{\partial y}\right)^2}}{\left\lvert\frac{\partial f}{\partial z}\right\rvert}\right]$	Radian	Cooper and Cowan (2006)
ITDX	$\tan^{-1}\left(\frac{\sqrt{\left(\frac{\partial^2 f}{\partial z \partial x}\right)^2 + \left(\frac{\partial^2 f}{\partial z \partial y}\right)^2}}{\left\lvert\frac{\partial^2 f}{\partial z^2}\right\rvert}\right)$	Radian	Ma et al. (2016)
LTHG	$\left[1 + \exp\left(-\frac{\mathrm{THDR}_z}{\sqrt{(\mathrm{THDR}_x)^2 - (\mathrm{THDR}_y)^2}}\right)\right]^{-\alpha}$	/	Pham et al. (2019)
ILTHG	$\left[1 + \exp\left(-\frac{\mathrm{ITHG}_z}{\sqrt{(\mathrm{ITHG}_x)^2 - (\mathrm{ITHG}_y)^2}}\right)\right]^{-\alpha}$	/	Melouah and Pham (2021)
TAHG	$\tan^{-1}\left(\frac{\mathrm{THDR}_z}{\sqrt{(\mathrm{THDR}_x)^2 + (\mathrm{THDR}_y)^2}}\right)$	Radian	Ferreira et al. (2013)
MNTH	$\tan^{-1}\left[\frac{\mathrm{ASA}}{\left\lvert\frac{\partial f}{\partial z}\right\rvert}\right]$	Radian	Pham (2023)
HTHG	$\tanh\left[\frac{\mathrm{THDR}_z}{\sqrt{(\mathrm{THDR}_x)^2 + (\mathrm{THDR}_y)^2}} - \frac{\pi}{2}\right]$	/	Ai, Ekinci, et al. (2024)

Note. Only the TM method indicate the edges by the minimal amplitude, the rest eleven methods identify the horizontal boundaries via the maximal amplitude.

$$\Delta g(x,y) = \gamma \Delta g \int_{z1}^{z2} \int_{y1}^{y2} \int_{x1}^{x2} \frac{z}{[x^2 + y^2 + z^2]^{1.5}} \mathrm{dxdydz} \tag{14}$$

where $\Delta\rho$ and γ are the density contrast and gravitational constant, respectively. x and y denote the horizontal coordinates of the source, and $z1$ and $z2$ denote the depths to the top and bottom of the source, respectively. The 3D model consists of five prisms, with their properties listed in Table 2.

Figures 1a and 1b present different views of the synthetic model. Synthetic data for these prisms were computed on an observation surface covering a 200 km^2 × 200 km^2 area, with a sampling interval of 1 km, following the derived formulation from Equation 14 reported by Rao et al. (1990). Figure 1c stores the noise-free gravity anomaly.

$$\tilde{d}_{\mathrm{syn}} = d_{\mathrm{syn}} + NR \times \mathrm{mean}[d_{\mathrm{syn}}] \times [\mathrm{rand}_1(M) - \mathrm{rand}_2(M)] \tag{15}$$

where mean [] is the average of the input data (d_{syn}), here we use the noise-free data as the input, and rand$_1$ () and rand$_2$ () generate pseudorandom values uniformly distributed between [0, 1], of a given size M.

To replicate real-world conditions, noise was introduced into the synthetic data in accordance with Equation 15 following the work of Ai, Ekinci et al. (2023) and Ai et al. (2025). This addition was considered critical for

Table 2
Model Parameters of the Prisms Used in the Synthetic Case

Model parameters	P1	P2	P3	P4	P5
X coordinate of the center (km)	20	100	130	110	110
Y coordinate of the center (km)	100	100	100	180	20
Width (km)	25	70	80	12	12
Length (km)	150	70	80	20	15
Thickness (km)	5	3	4	2	1.5
Depth to the top (km)	2	1	3	2	4
Strike (°)	0	45	45	0	0
Density contrast (kg/m^3)	500	−250	500	300	−300

evaluating the robustness of the edge detectors, particularly due to the noise amplification commonly observed in derivative-based calculations.

$$Re = \frac{\left\| \tilde{d}_{\text{syn}} - d_{\text{syn}} \right\|}{\left\| d_{\text{syn}} \right\|} \times 100 \tag{16}$$

The noise ratio (NR) in Equation 15 is a predefined parameter that governs the noise level, set to $NR = 20\%$ in this study, yielding an approximate relative error (Re) of 6%, as determined by Equation 16 (Ai, Ekinci et al., 2023).

The correlation coefficient between the noise-free and noisy data is 0.998, indicating that the random noise has a slight impact on the data. The noise-perturbed gravity anomaly is presented in Figure 1d. Using the generated noise-free and noisy gravity anomalies, the 12 edge detectors were first applied to the noise-free data to assess their effectiveness. Figure 2 shows the outputs of each operator. Blue triangles indicate the boundaries of the synthetic bodies.

The results demonstrated that the THDR is predominantly influenced by the high-amplitude effect from the shallow source P1, which is the thickest one. This enhances the delineation of the boundary of P1, while the boundaries of the deeper sources, P4 and P5, with lower amplitudes, are less distinct and exhibit blurring. Similar to THDR, ASA effectively highlighted the shallow sources (e.g., P1 and P2) but is less effective in clearly defining the boundaries of the deeper sources. This finding indicated that THDR and ASA are primarily effective for detecting shallow structures with considerable vertical extents. The TA detector exhibited difficulty in precisely delineating horizontal boundaries when anomalies are generated by sources with both positive and negative density contrasts. Spurious edges were detected around P2, P3, and P4. Similarly, false edges were noticed with

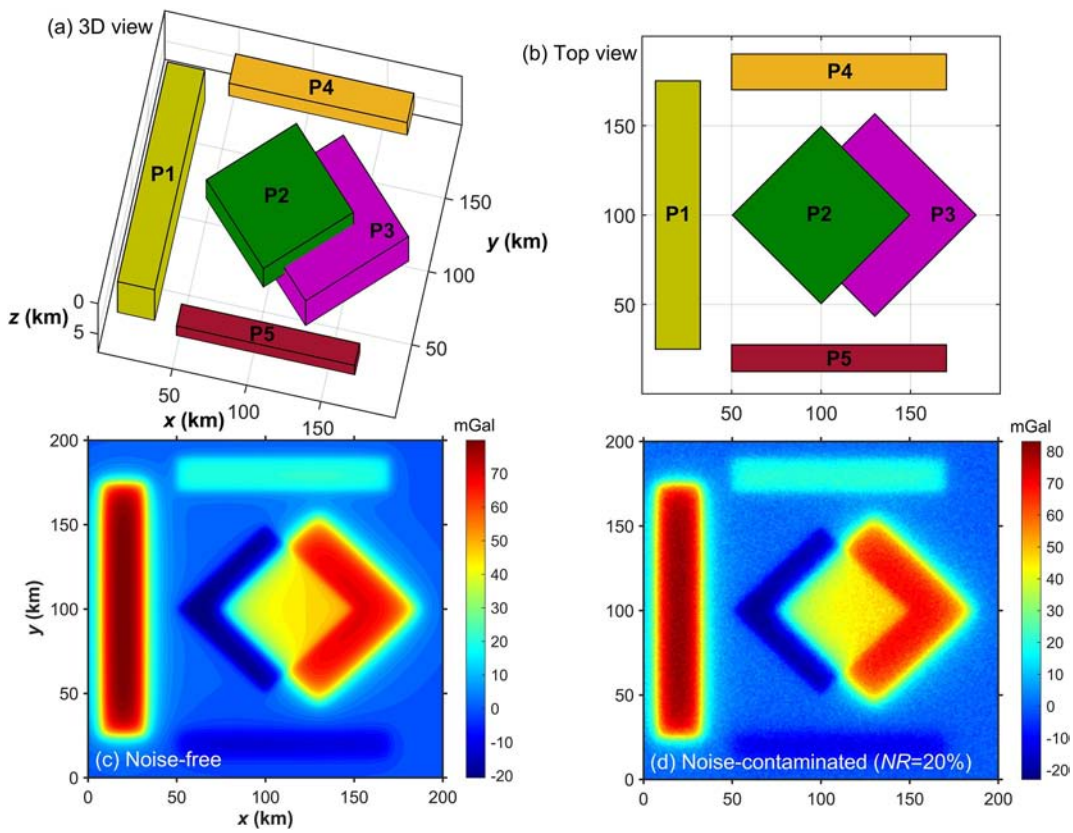

Figure 1. (a) Side view of the synthetic model, (b) Top view of the synthetic model, (c) The generated noise-free data, (d) The noise-contaminated gravity anomaly ($NR = 20\%$, but generates a ~6% relative error to the clean data).

10.1029/2025EA004379

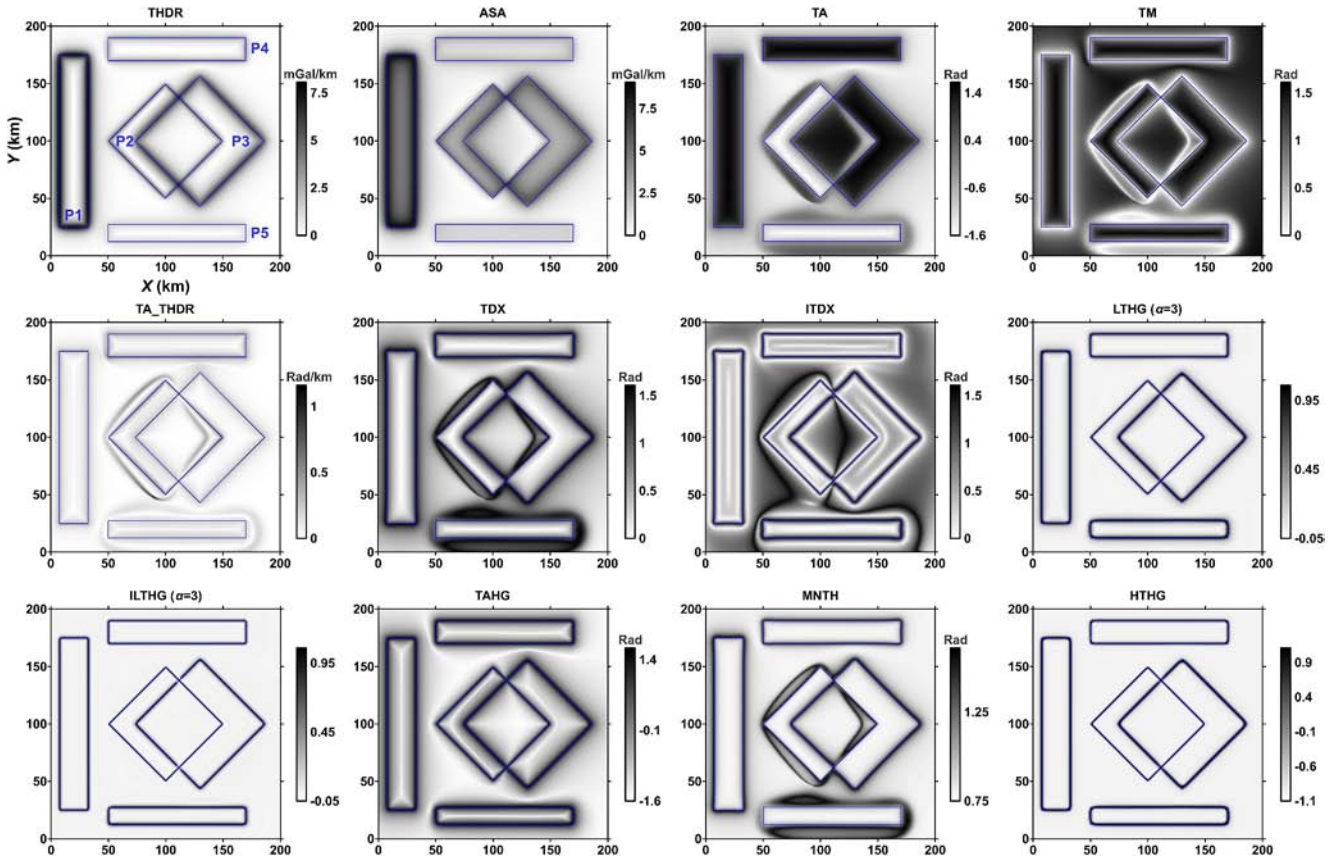

Figure 2. Outputs of the edge detectors applied to the synthetic noise-free gravity anomaly shown in Figure 1c. Blue rectangles denote the edges of the prisms.

other detectors (TM, TA_THDR, TDX, ITDX, and MNTH), highlighting the inability of these operators to effectively resolve both positive and negative amplitude contrasts. However, most of these approaches yielded relatively well-balanced, high-resolution results, with the exception of TA_THDR, which produced ambiguous outcomes. Furthermore, TAHG displayed fewer compact responses, with their peak amplitudes surrounded by diffusive, weaker signals.

LTHG, ILTHG, and HTHG demonstrated superior performance in delivering the most pronounced and well-resolved responses for source boundaries. However, it should be noted that the effectiveness of the LTHG and ILTHG detectors is contingent upon the user-defined parameter α. Here, $\alpha = 3$ was used to achieve the satisfactory result, while the performance of the two methods controlled by different α values will be discussed later.

Comparatively, HTHG operated without parameter adjustments, making it the most robust method for processing noise-free gravity data.

Figure 3 illustrates the results of applying these operators to the synthetic gravity data with simulated noise ($NR = 20\%$; data in Figure 1d), providing a more comprehensive evaluation of their performance. As expected, all detectors were influenced by the amplified noise from the derivative calculation process, despite the relatively low noise magnitude ($Re = 6\%$). Normalization-based filters and high-order derivative methods exhibited remarkably poorer performance, with ILTHG retaining only minimal useful edge information compared to LTHG and HTHG. This finding highlighted the critical need for noise reduction strategies before the applications of these types of operators to preserve edge detectability in the presence of noisy data.

Several noise reduction strategies were developed to stabilize derivative computations, such as the backward finite difference (BFD) approach (Florio et al., 2006; details of this method are given in Appendix A), the fourth-order Tran-Nguyen (FTN) formula (Tran and Nguyen, 2020; details of this method are given in Appendix B), and the β-vertical derivative (β-VDR; details of this method are given in Appendix C) method (Oliveira and

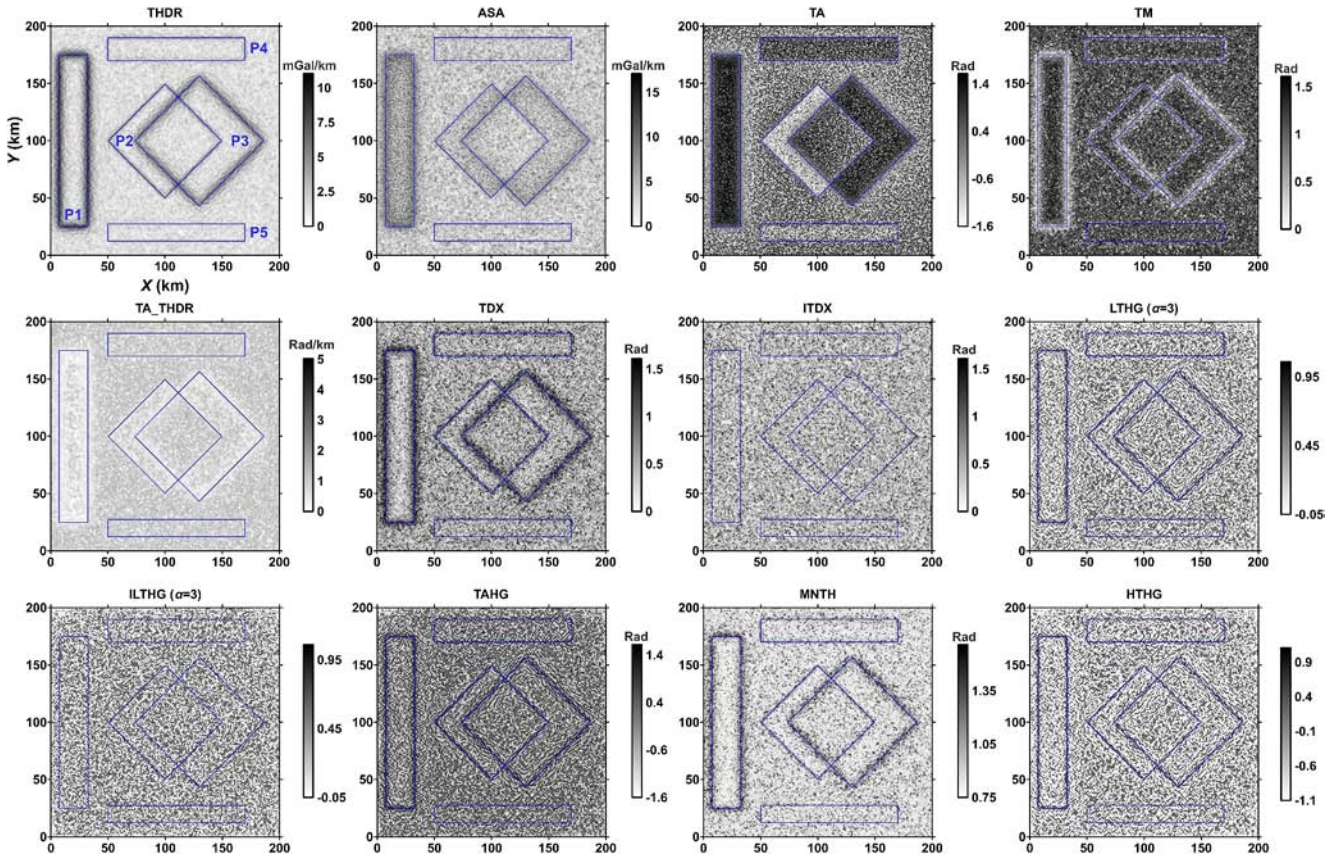

Figure 3. Outputs of the edge detectors applied to the synthetic noisy gravity anomaly shown in Figure 1d. Blue rectangles denote the edges of the prisms.

Pham, 2022). Additionally, the non-local means (NLM) function (Buades et al., 2011) and modified NLM (MNLM) (Ai, Alvandi, et al., 2023; details of this method are given in Appendix D) were proposed prior to derivative calculations as noise reduction filters.

BFD, FTN, and β-VDR, basically, are generated using finite difference theory, which yields the capability of suppressing the small-scale noise during the derivative calculation process. MNLM, on the contrary, attenuates the small-scale noise prior to the differentiation process via parameter tuning and spatial convolution. The performance of each filtering operator is affected by its respective control parameters, which are distinct for each approach: h for BFD and FTN, β for β-VDR, and H for MNLM. However, none of the previous works gave detailed analyses on the parameter tuning quantitatively or qualitatively.

Within this work, following the available works of determining regularization parameters, the Lp ($p = \{1;2\}$; see Pašteka et al., 2012) norms and C norm (a special form of the Lp norm regarding Karcol and Pašteka (2025)) are used as tools for such tuning parameter estimation. Notably, the tuning parameters of the BFD, FTN, β-VDR, and MNLM methods are different from the optimization frame of regularization methods. We thus innovatively used the Lp norms and C norm to tune these control parameters.

Basically, the Lp norms and C norm are calculated via the difference between two consecutive solutions calculated for the pre-determined tuning parameter sequence. Refer to the works of Pašteka et al. (2012) and Karcol and Pašteka (2025) for more details.

Definitely, the trial-and-error method is still valid and commonly used. Except for the mentioned approaches for determining the tuning parameter, there are several other methods including: Shape of Anomaly curve (René, 1986), Generalized Cross Validation method (Wahba, 1990), L curves (Hansen, 1994) or Variance Component Estimation method (Kusche and Klees, 2002), which will not be discussed here.

10.1029/2025EA004379

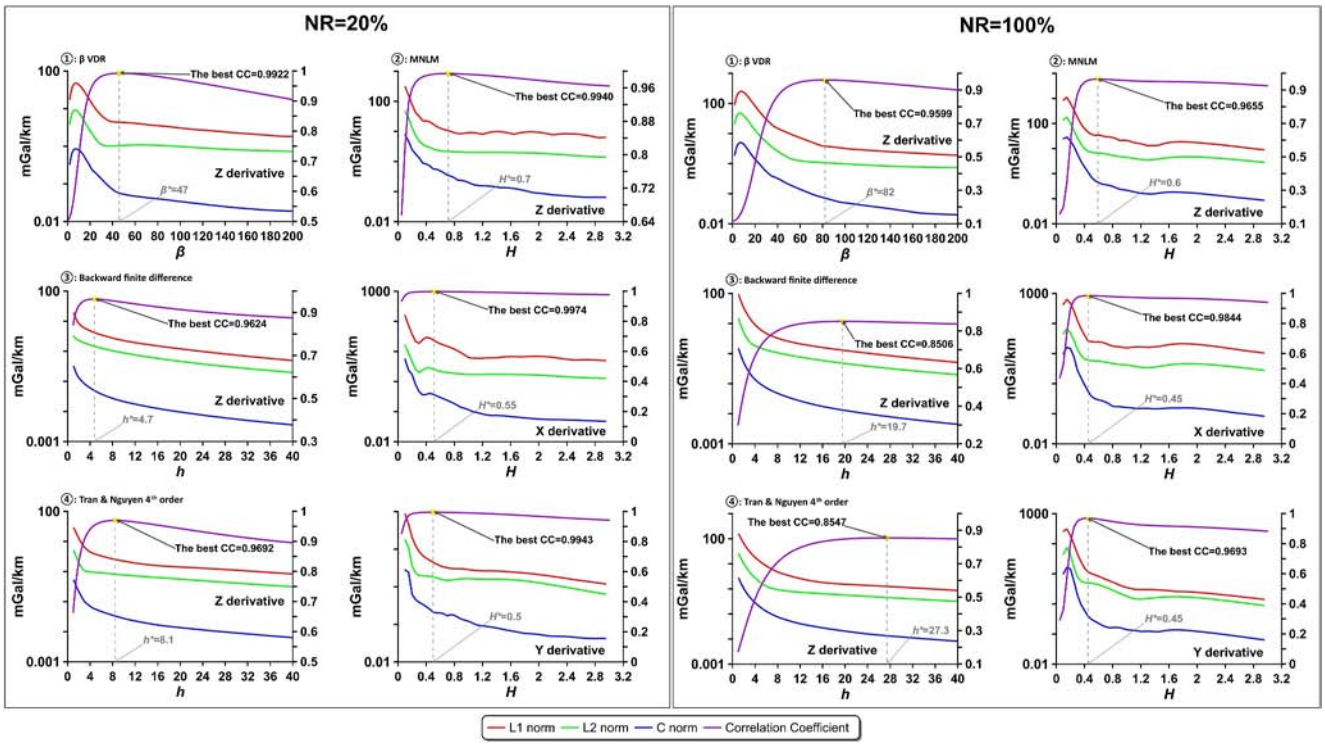

Figure 4. The calculated Lp norms and C norm of the β-VDR, BFD, FTN, and MNLM methods varying with the control parameter coping with the synthetic noisy data with different noise ratios ($NR = 20\%$ related to the left two columns and $NR = 100\%$ related to the right two columns). The red, green, blue, and purple curves denote the variation of the values calculated using L1 norm, L2 norm, C norm, and CC. The left axis presents the values of the Lp norms and C norm, and the right axis stores the values of the CC value.

3.1. Synthetic Tests With Different Noise Levels

To assess the performance of the involved four noise attenuation methods, we perform BFD, FTN, β-VDR, and MNLM on the noise-corrupted response with different levels ($NR = 20\%$ and $NR = 100\%$). Notably, within this study, BFD, FTN, and β-VDR are solely implemented to calculate the vertical derivative as previously implemented within the study of Oliveira and Pham (2022). The MNLM can be used to suppress noise related to derivatives of different directions, as it is a spatial filter prior to the derivative calculation process.

For the synthetically generated noisy cases, we can actually identify these quasi-optimal control parameters by locating the maximal correlation coefficient (CC) factor calculated using the derivatives from the noise-free and denoised data controlled by different tuning parameters. However, for the subsequent field cases, the CC factor is absent due to the absent pure noise-free field data set.

Figure 4 stores the calculated Lp norms and C norm of the involved four noise suppression methods, with the CC value varying with the control parameter. The left and right two columns exhibit the results of the $NR = 20\%$ and $NR = 100\%$ cases, respectively. The parameter β was varied from 1 to 200 in increments of 1, h was adjusted from 1 to 40 with a step size of 0.1, and H was tuned from 0.05 to 3 in increments of 0.05. The red, green, blue, and purple curves denote the variation of the values calculated using L1 norm, L2 norm, C norm, and CC. Notably, the left axis in Figure 4 presents the values of the Lp norms and C norm, and the right axis stores the values of the CC value. Within the two noisy cases, the left column shows the Lp norms and C norm regarding the BFD, FTN, and β-VDR methods on the vertical derivative calculation. The right column gives the four curves of the MNLM method with respect to the three directions' derivative calculation.

Generally, the results presented in Figure 4 suggested that denoising performance is strongly related to the parameter tuning process, rather than by arbitrarily applying large values. Larger values effectively reduced noise, but they also attenuated shorter wavelength details, resulting in less favorable outcomes (Ai, Alvandi, et al., 2023).

Based on the work of Pašteka et al. (2009) and Karcol and Pašteka (2025), we can identify the estimation of the tuning parameter by locating the local minimum within the Lp norms and C norm. However, there are no local minima at all within the Lp norms and C norm. These curves rather yield the similar features of the "L" curve.

We thus can roughly determine the regularization parameter according to the "elbow" part of the L curve when dealing with field cases by performing the denoising processing with some of the values within the biggest curvature range.

Speaking of the CC curve, the variation shown in Figure 4 is small within the near side of the maximum CC values. Based on the highest correlation coefficients across different *NR* levels, MNLM exhibited the best performance regarding the vertical derivative, achieving maximum correlation coefficients of 0.994 and 0.9655 for *NR* levels of 20% and 100%, respectively.

β-VDR performed slightly below MNLM, yielding correlation coefficients of 0.992 and 0.9599 for the same *NR* levels. The BFD approach exhibited the weakest performance among the evaluated approaches. Applications revealed that the optimal β value increases with rising noise levels, reaching 47 and 82 for the respective *NR* levels. In contrast, the optimal *H* value decreased as noise intensity increased, with corresponding values of 0.7 and 0.6. This trend is attributed to the definition of *H* in MNLM, where it serves as a ratio relative to the magnitude of the noisy data. At higher noise levels, the "min (max (∼))" term increases, necessitating a smaller *H* value to effectively suppress noise while preserving small-scale details.

Furthermore, the tuning parameter of MNLM is much less sensitive to the noise levels compared to the rest of the denoising methods. The "elbow" part of these curves within the other three methods yields a more pronounced discrepancy with the maximal CC values, indicating the effectiveness of the three methods cannot be guaranteed when dealing with more complex situations.

These features make MNLM a robust method for suppressing randomly distributed noise. Especially in the application of field cases, there is no CC curve that can maximize the performance of MNLM; the discrepancy of selecting the optimal tuning parameter will degrade the performance of MNLM. But, regarding the fact that the "elbow" part of these curves yields high consistency, the maximal CC value and the CC curve barely change within a big range of the "elbow" part. The quasi-optimal tuning parameter thus will not heavily contaminate the performance of MNLM.

Next, for the first noisy data ($NR = 20\%$), the 12 edge detectors were applied to the denoised data via MNLM with the tuning parameter shown in Figure 4. The results (Figure 5) validate the effectiveness of noise attenuation in improving edge detection performance. Among the edge detectors, HTHG yielded the most distinct and well-defined edge information with minimal noise, while LTHG ($\alpha = 3$) also performed effectively but generated small-amplitude artifacts around the maximal amplitude parts that hindered accurate edge identification. In contrast, ILTHG ($\alpha = 3$) exhibited weak performance, with its sharp edges covered by substantial noise artifacts.

The performance of the filters was further evaluated by utilizing the β-VDR method to mitigate noise during the application of the edge detectors. The tuning parameter of β-VDR was also determined via the Lp norms and C norm as mentioned above. In this case, the effectiveness of HTHG was reduced, and the edge of P4 was scarcely identifiable, although the noise level remained lower compared to the other methods (Figure 6). While ILTHG and LTHG were able to reveal rough edge information, their performance was undermined by noise artifacts. A comparison between Figures 5 and 6, particularly the HTHG results obtained from data denoised with MNLM and β-VDR, reveals that MNLM offers superior noise suppression with the same parameter tuning strategy. The combination of MNLM and edge detection approaches yielded improved results by reducing noise amplification during the derivative calculation process, thereby preserving the success of the edge detectors. For simplicity, the performance of integrating the other two denoising methods dealing with the synthetic noisy data will not be discussed here because the maximal CC values shown in Figure 4 already proved the other two methods are not satisfactory.

3.2. The Control Parameter Effect of the LTHG and ILTHG Methods

As mentioned above, the control parameter α affects the performance of the detected results achieved by the LTHG and ILTHG methods. Figure 7 exhibits the detailed performance of the LTHG and ILTHG methods with the control parameter $\alpha = 1$ and 5 under different situations. Regarding all the results presented in Figure 7, we

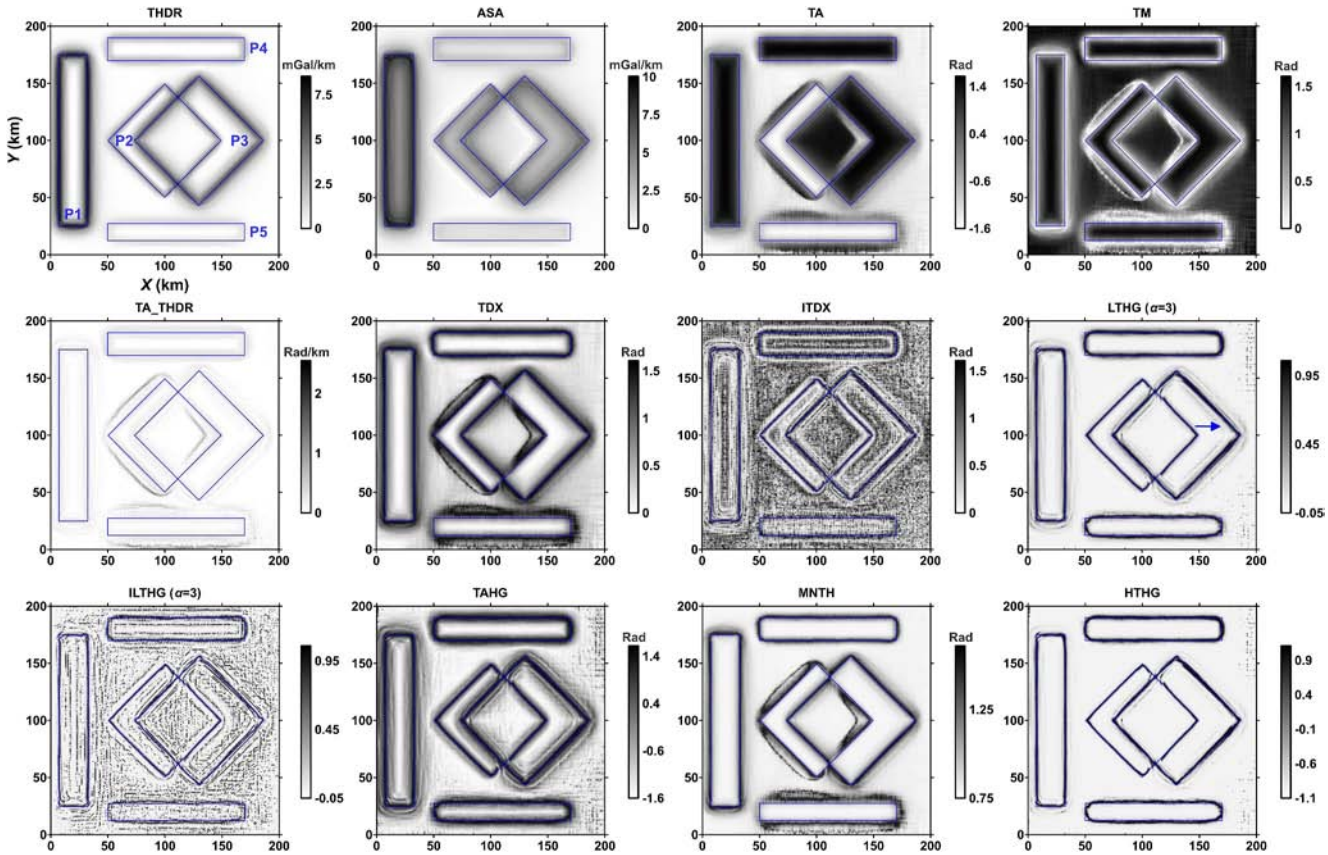

Figure 5. Results from the edge detectors used on the synthetic gravity anomaly with $NR = 20\%$, which was denoised using MNLM ($Hz = 0.7$, $Hy = 0.5$, $Hx = 0.55$ for the three directions). Blue rectangles denote the edges of the prisms.

can see that the LTHG and ILTHG with $\alpha = 1$ give unwanted performance with annoying interfering artifacts compared with the situation of the LTHG and ILTHG methods with $\alpha = 5$. Notably, the noise or remaining noise from the imperfect denoising procedure also significantly contaminates the results of the two methods. These features proved also the necessity of using a suitable noise attenuation method during the implementation of the edge detection methods.

Comparing Figures 5–7, LTHG is capable of achieving satisfactory results as the HTHG method as long as $\alpha > 1$ and suppressing the small wavelength information via MNLM when dealing with more practical situations compared with ILTHG. ILTHG performs unsatisfactorily when the input data contains interfering information regardless of the tuning parameters used. To the best of our knowledge, this is also the first study of integrating the MNLM with LTHG to enhance the performance of LTHG when the data is noise-contaminated.

Additionally, as the α increases, the edge information of LTHG will be more compact and thin (but small-magnitude interfering artifacts around the authentic edges are still observable), which may be useful when dealing with some cases needing ultra-high resolution.

But in our case, we prefer the utilization of HTHG without any control parameter but still can generate robust and clear edge information. Less control parameter involvement will achieve more objective results.

3.3. The Downsampled Data Effect

Speaking of real-world applications, the resolution of the obtained data also matters. Figure 8 presents the calculated Lp norms and C norm of the β-VDR, BFD, FTN, and MNLM methods varying with the control parameter coping with the downsampled noisy data ($NR = 20\%$; the downsampled data size is 51×51 instead of 201×201). The best CC values of the MNLM case vary slightly (still around 0.7), and they still obtain good consistency of the "elbow" of these curves; however, the best tuning parameters of the other three methods yield

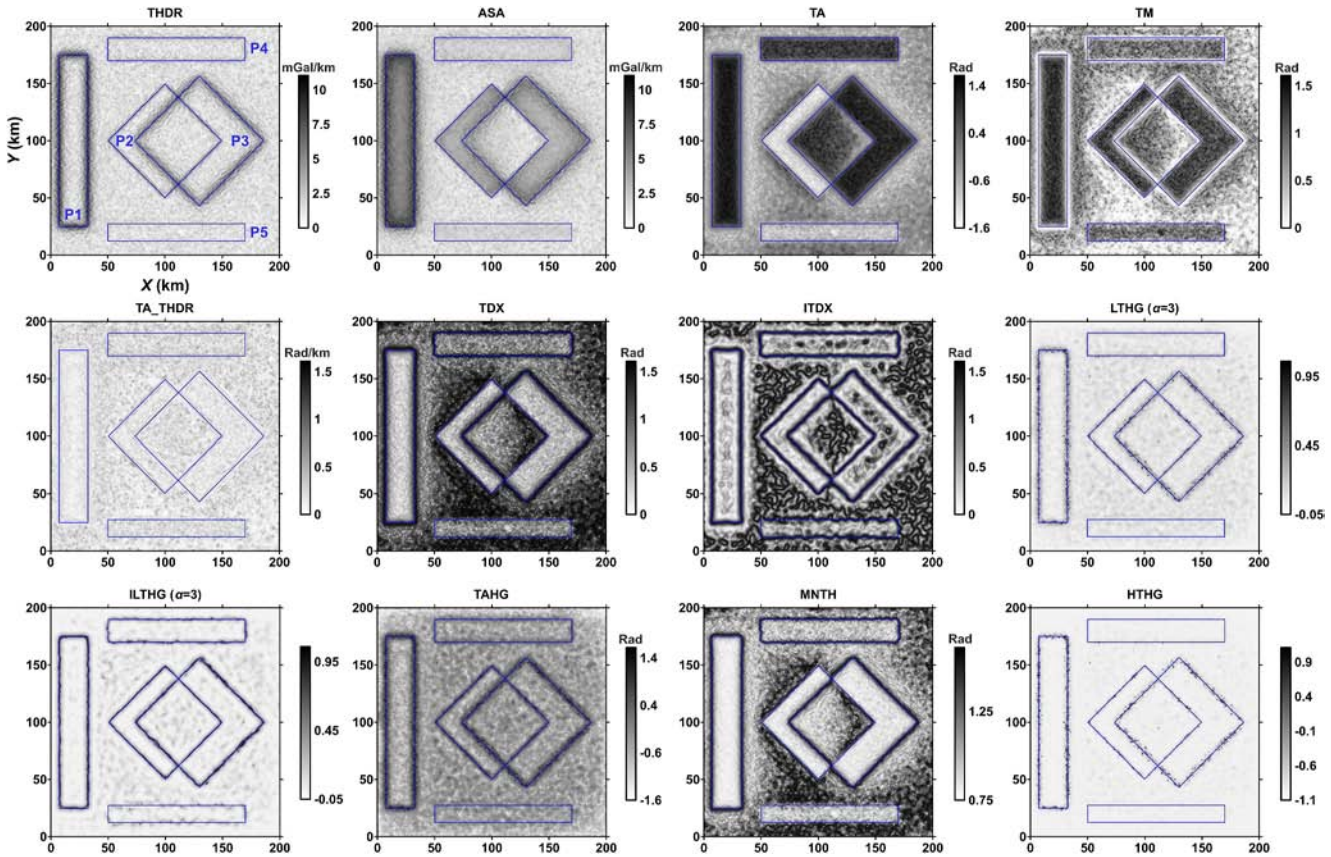

Figure 6. Outputs of the edge detectors applied to the synthetic gravity anomaly denoised using β-VDR ($\beta = 47$). Blue rectangles denote the edges of the prisms.

significant changes compared to that of the noisy data case with $NR = 20\%$ and a data size of 201×201. More importantly, the "L" curve-like feature vanishes, which increases the difficulty of identifying these parameters. These phenomena are similar to the aforementioned features related to Figure 4. In conclusion, MNLM outperforms the other three noise attenuation methods regardless of the noise levels and data size. Its tuning parameter can be robustly determined via the "elbow" part of the Lp curves and C norm.

3.4. The Regional Anomaly Effect

One of the biggest problems in dealing with potential field data is the elimination or separation of regional information. This section is dedicated to investigating the regional effect on edge detection. Equations 17–20 present the simulation of the regional effect $\tilde{d}_{\mathrm{reg}}$ with the basic assumption that the regional information can be approximated by polynomials (Ai, Ekinci et al., 2023). This simulation is acceptable, as many regional information suppression methods are based on different orders of polynomials (Chen et al., 2024).

$$d_{\mathrm{regx}} = 10^{-5}X^3 + 10^{-6}X^2 + 10^{-5}X^1 - 10 \tag{17}$$

$$d_{\mathrm{regy}} = -10^{-5}Y^3 - 10^{-6}Y^2 - 10^{-5}Y^1 - 10 \tag{18}$$

$$d_{\mathrm{reg}} = d_{\mathrm{regx}} + d_{\mathrm{regy}} \tag{19}$$

$$\tilde{d}_{\mathrm{reg}} = d_{\mathrm{reg}}^{\mathrm{normalized}} \times \mathrm{mean}(d_{\mathrm{syn}}) \times 3, d_{\mathrm{reg}}^{\mathrm{normalized}} = [d_{\mathrm{reg}}/\max(d_{\mathrm{reg}})]. \tag{20}$$

X and Y here denote the horizontal coordinates of the calculation grid. Correspondingly, Figure 9a shows the generated regional anomaly, and Figure 9b gives the most practical simulation of the real-world potential field

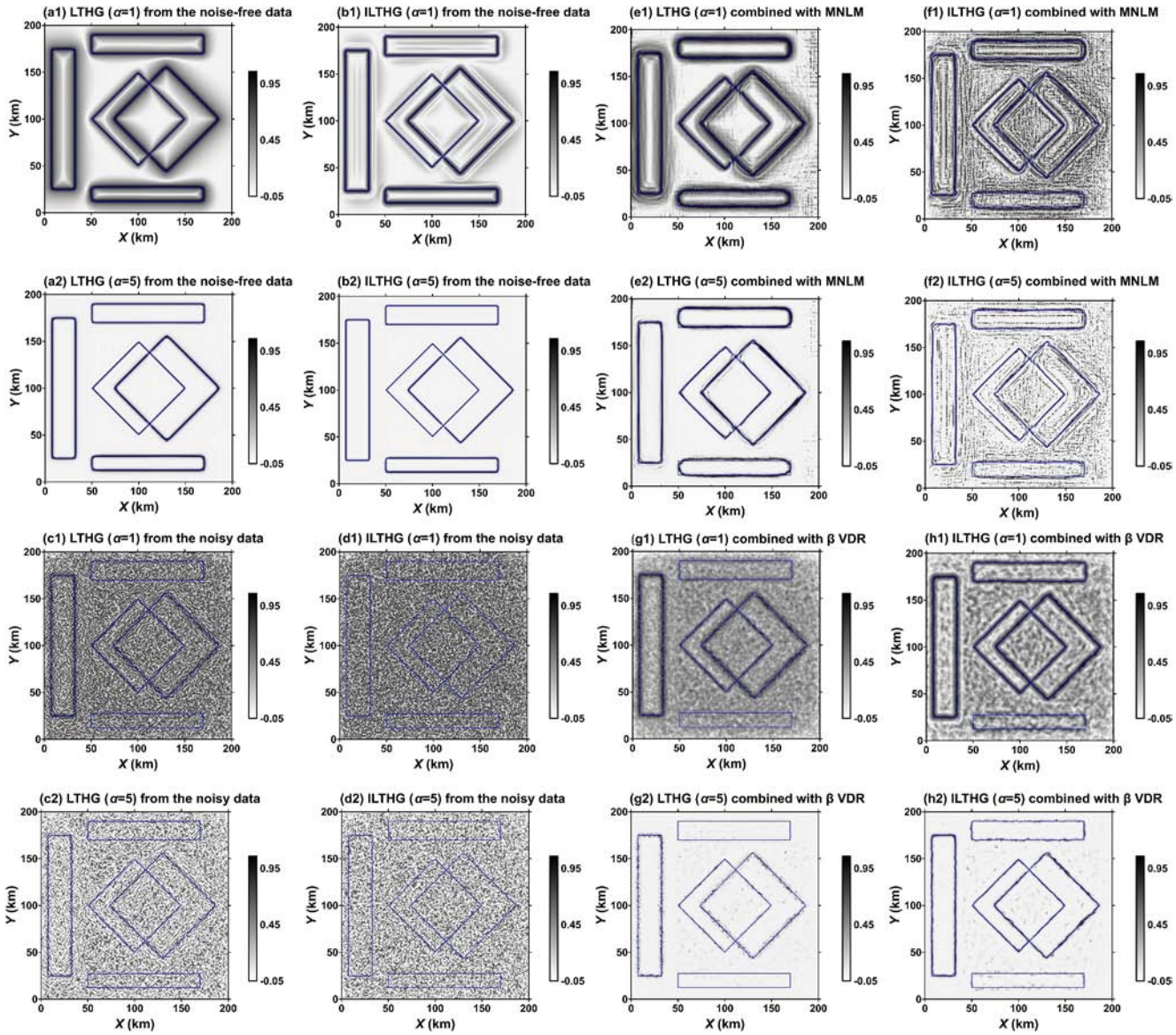

Figure 7. The performance of the LTHG and ILTHG methods with the control parameter $\alpha = 1$ and 5 under different situations. (a1)–(b1) shows the results of the two methods dealing with the noise-free data with $\alpha = 1$. (a2)–(b2) illustrates the results of the two methods dealing with the noise-free data with $\alpha = 5$. (c1)–(d1) stores the results of the two methods dealing with the noisy data ($NR = 20\%$) with $\alpha = 1$. (c2)–(c2) illustrates the results of the two methods dealing with the noisy data ($NR = 20\%$) with $\alpha = 5$. (e1)–(f1) exhibits the results of the two methods dealing with the denoised data via MNLM with $\alpha = 1$. (e2)–(f2) exhibits the results of the two methods dealing with the denoised data via MNLM with $\alpha = 5$. (g1)–(h1) exhibits the results of the two methods dealing with the denoised data via β-VDR with $\alpha = 1$. (g2)–(h2) exhibits the results of the two methods dealing with the denoised data via β-VDR with $\alpha = 5$. Blue rectangles denote the edges of the prisms.

data. That is, the gravity anomaly from the synthetic model further contains regional effects and random noise ($NR = 20\%$). Figures 9c and 9d exhibits the side views of (a) and (b), respectively.

With the simulated data in Figure 9b, if we directly perform the involved 12 edge detectors on the data, the results will share no big difference with that of Figure 3 due to the random noise amplification problem during the derivative calculation. We thus first attenuate the random noise using MNLM within Figure 9b and apply the 12 edge detection methods on the gravity anomaly with regional effect and the remaining noise from the MNLM denoising process to investigate the regional anomaly effect. Moreover, basically, if the regional anomaly is a constant, the involved 12 edge detection methods will not be influenced due to the derivative calculation. But the regional information simulated by the third-order polynomials may erode the performance of some edge detectors.

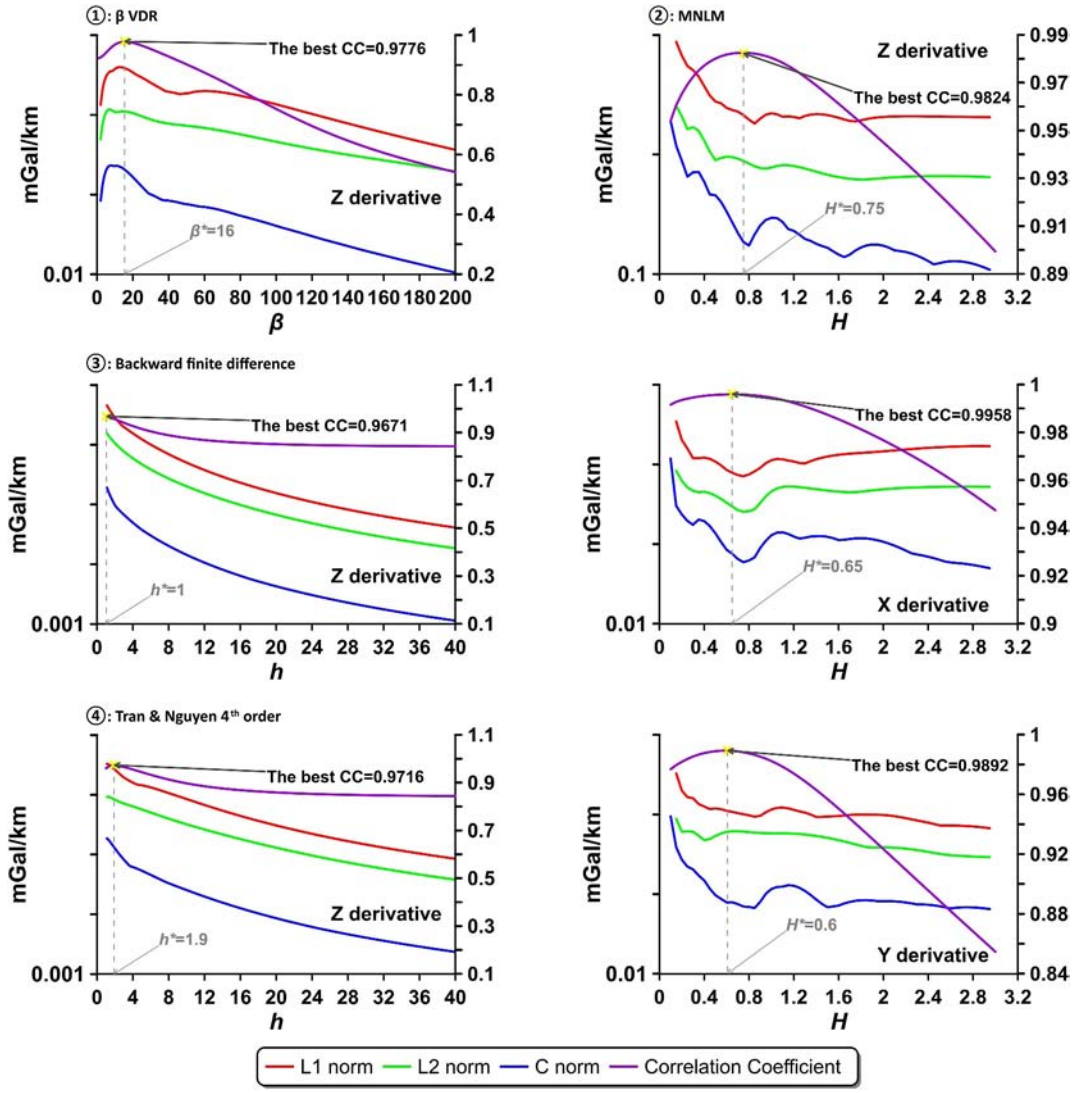

Figure 8. The calculated Lp norms and C norm of the β-VDR, BFD, FTN, and MNLM methods varying with the control parameter coping with the downsampled noisy data ($NR = 20\%$; the downsampled data size is 51×51 instead of 201×201). The red, green, blue, and purple curves denote the variation of the values calculated using L1 norm, L2 norm, C norm, and CC. The left axis presents the values of the Lp norms and C norm, and the right axis stores the values of the CC value.

Figure 10 contains the outputs of the 12 edge detectors (the tuning parameter of the LTHG and ILTHG methods is still $\alpha = 3$) applied to the synthetic gravity anomaly with regional effect with random noise attenuated by MNLM. Comparing Figures 5 and 10, the regional information left obvious artifacts within the results of the TM, TDX, and MNTH (see the pointed parts via blue arrows). Other results are similar to that of Figure 5 with unnoticeable information from the regional anomaly. Notably, HTHG and LTHG methods yield the most satisfactory results with clear, unaffected, and well-balanced amplitude edge information and with mild interrupting information at the right boundary. But in further comparison, LTHG contains more obvious small-amplitude artifacts around the authentic edges, as the blue arrow indicates. We can thus conclude the HTHG method is not significantly affected by the regional anomaly simulated by third-order polynomials due to the effective combination of different orders of derivatives.

4. Applications With the Aristarchus Plateau Gravity Data

The synthetic experiments underscored the efficacy of the HTHG method in outlining the lateral boundaries of subsurface geological structures. Consequently, the HTHG detector was applied to lunar gravity data to map the

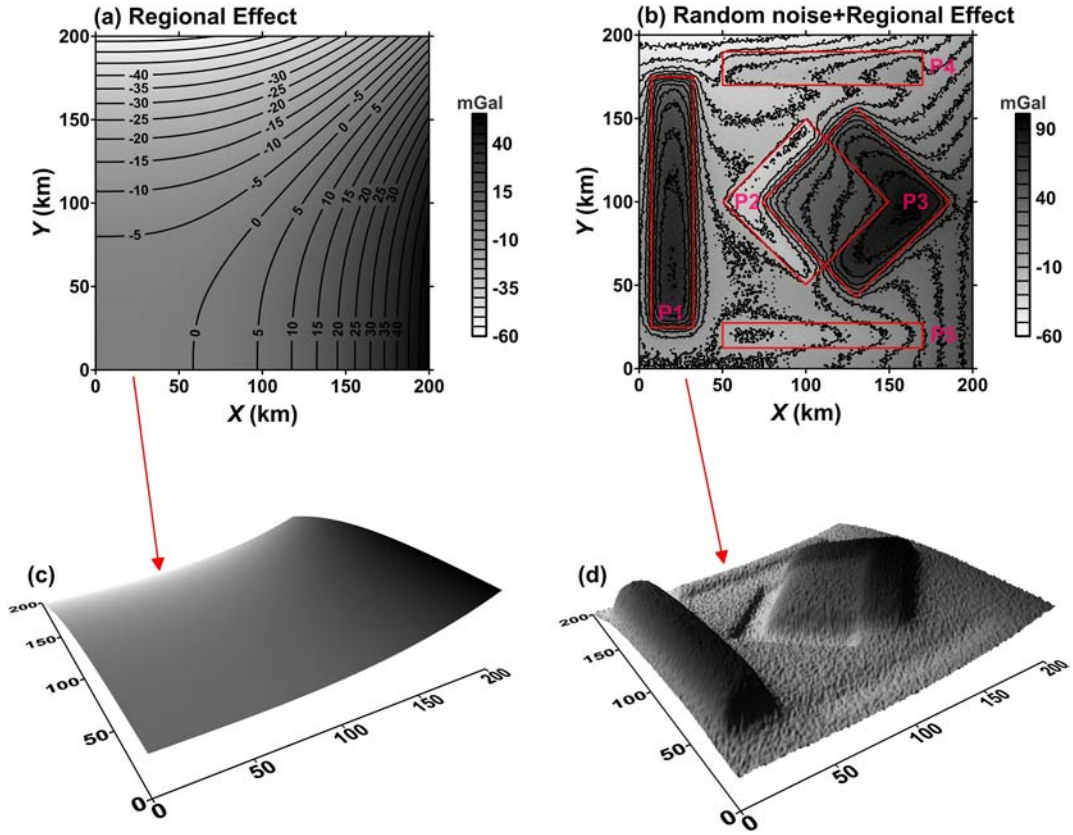

Figure 9. (a) The generated regional anomaly, (b) The gravity anomaly from the synthetic model further contains regional effect and random noise ($NR = 20\%$), (c) Side view of the regional anomaly, and (d) Side view of (b). P1–P5 in (b) are the labels of the five buried sources. Red rectangles denote the edges of the prisms.

abrupt lateral density variations within the Aristarchus plateau. The topographic and Bouguer gravity data sets utilized here were obtained from Liang et al. (2024). In their study, the digital elevation model of the moon was used. Additionally, Liang et al. (2024) performed a morphological analysis using SELENE terrain camera data (10 m/pixel). The free-air and Bouguer gravity data were obtained from the lunar gravity model GRGM1200L (Goossens et al., 2020). Liang et al. (2024) eliminated spherical harmonic degrees and orders below six from the model to underscore small-scale effects. To further minimize other interfering effects, they also removed harmonic coefficients above degree 660. The Bouguer gravity anomalies were calculated by subtracting the topographic effect from the free-air gravity anomaly. Figures 11a and 11d demonstrate the topographic and Bouguer gravity maps of the Aristarchus plateau, respectively, as derived from Liang et al. (2024). A prominent negative anomaly within the uplifted block of the plateau is clearly seen. This response is most likely associated with the presence of a deep mountain root. Figures 11b and 11c display the profiles extracted from the topographic data, whereas Figures 11e and 11f illustrate the associated Bouguer gravity anomalies.

We began with the application of 12 aforementioned edge detectors to the lunar gravity anomalies without any small wavelength information reduction. Figure 12 demonstrates the outcomes of the detectors. These edge detection results are not heavily corrupted by the amplified small wavelength information during the derivative calculation process, which indicates the spherical harmonic analysis is also a useful tool to suppress unwanted interfering information. Consistent with Figure 2, the detected boundaries share similar characteristics. The THDR operator predominantly highlighted large-amplitude anomalies, pointing to the potential existence of shallow sources beneath the Aristarchus crater. The ASA operator indicated a significant mass beneath the crater and to the south; however, both THDR and ASA are insufficient for accurately identifying deeper sources. The TA detector exhibited lengthy and spurious boundaries, while TM, TDX, ITDX, and MNTH generated some artifacts that hindered the identification of meaningful edge information. The TA_THDR approach provided a limited and imbalanced outcome. The LTHG ($\alpha = 3$) and HTHG detectors demonstrated superior performance

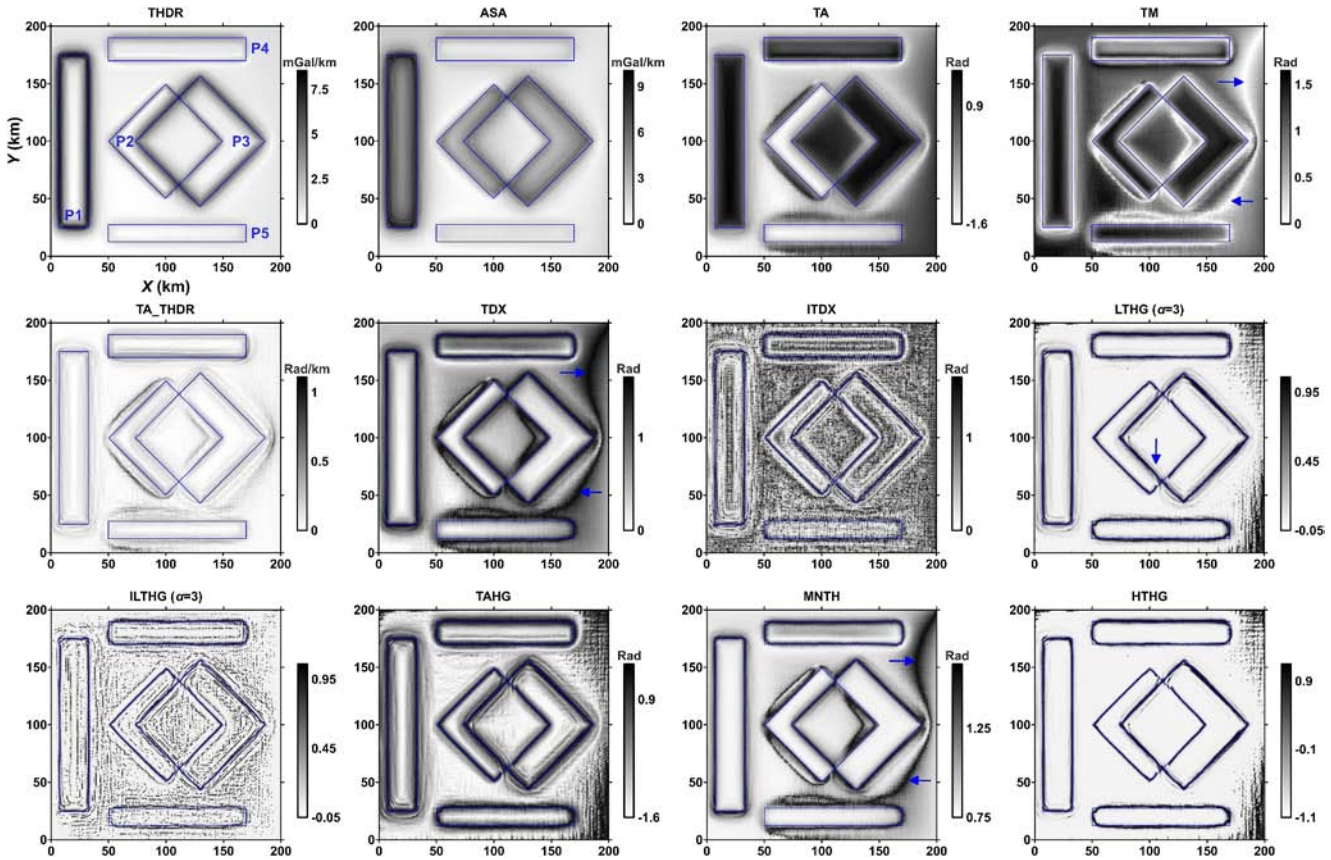

Figure 10. Outputs of the edge detectors applied to the synthetic gravity anomaly with regional effect with random noise attenuated by MNLM. Blue rectangles denote the edges of the prisms.

compared to the ILTHG ($\alpha = 3$) and TAHG approaches, as they produced edge information that is precise, well-defined, and readily identifiable.

The TAHG operator failed to achieve the necessary high resolution, while ILTHG generated an overabundance of small-scale features that impede effective boundary detection. In general, HTHG showed superior performance by delineating geological structure boundaries with clarity and negligible artifact contamination. While LTHG demonstrated acceptable performance, it produced edges with more pronounced small-magnitude "shadows," making the edge information less compact and credible than those generated by HTHG. This finding indicated superior capability of the HTHG detector in delineating geological boundaries at the Aristarchus plateau with proper spherical harmonic analysis.

Subsequently, we generated the edge detector outputs from the lunar gravity anomaly that had been denoised using the MNLM filter with the parameter tuned via the Lp norms and C norm (the results presented within the right column of Figure 13). *H* was tuned from 1 to 10 in increments of 0.5. The determined tuning parameters of MNLM are given within Figure 13. Notably, there is no correlation coefficient curve in dealing with real-world cases. A comparison between Figures 12 and 14 further demonstrated the importance of small wavelength noise reduction in edge detection, as even slight random noise can significantly distort edge detection solutions due to the amplification during derivative computations.

Among the detectors employed, HTHG generated the most well-defined structural boundaries with minimal noise interference (Figure 14), which further validates its superior performance observed in Figure 12. While LTHG also yielded good outcomes, it still introduced subtle shadow-like artifacts. ILTHG remained less effective than HTHG due to small-scale artifacts that distorted its sharp edge information. Other detectors demonstrated the previously observed limitations that make them less effective for detailed edge detection.

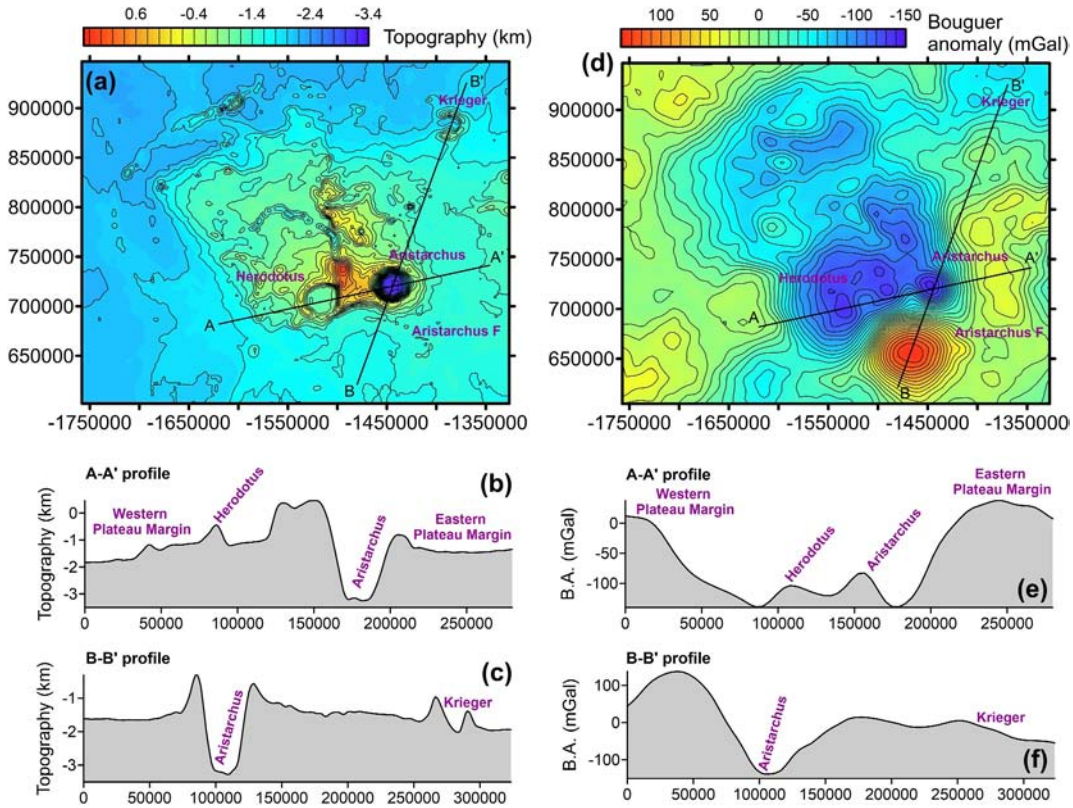

Figure 11. The topographic (a) and Bouguer gravity (d) data sets are obtained from Barker et al. (2016) and Liang et al. (2024). Two profiles (b and c) extracted from the topographic map and their corresponding gravity anomalies (e and f) are shown.

4.1. The α Effect of the LTHG and ILTHG Methods Regarding the Lunar Gravity Data

Consistent with the synthetic tests, we here also investigate the parameter-selecting effect on the LTHG and ILTHG methods. Figure 15 exhibits the performance of the LTHG and ILTHG methods dealing with the lunar gravity data with the control parameter $\alpha = 1$ and 5 under different situations. Regarding the results presented in Figure 15, the LTHG and ILTHG with $\alpha = 1$ also give unwanted performance with annoying interfering artifacts compared with the situation of the LTHG and ILTHG methods with $\alpha = 5$ as aforementioned within the synthetic tests.

Comparing Figures 14 and 15, LTHG achieved comparable results as the HTHG method with $\alpha = 5$. Even the subtle shadow-like artifacts are further suppressed when comparing the case of $\alpha = 3$ and $\alpha = 5$. However, speaking of the edge consistency, HTHG still performs better. Doubtlessly, ILTHG performs weaker in dealing with field data containing interfering information regardless of the tuning parameters used. With these features, we thus still can say HTHG yields the precious capability of generating robust, consistent, and clear edge information without any control parameter selecting, making it a valuable method for tackling more complex problems.

4.2. Comparison of the BFD, FTN, and β-VDR

As we already made clear, the HTHG method outperforms the rest of the edge detection techniques. Figure 16 shows a further comparison related to the HTHG method with the noise attenuation method of MNLM, β-VDR, BFD, and FTN, respectively. The parameters of the β-VDR, BFD, and FTN methods are also tuned regarding the Lp norms and C norm (depicted in the left column in Figure 13). The determined tuning parameters of the three methods are also denoted within Figure 13. It should be noted that the curves in the left column of Figure 13 show the vertical directions calculated for the THDR so that the HTHG method can be achieved regarding Equation 13. Other direction derivatives are obtained via the scripts within the work of Castro et al. (2018). But for MNLM, it

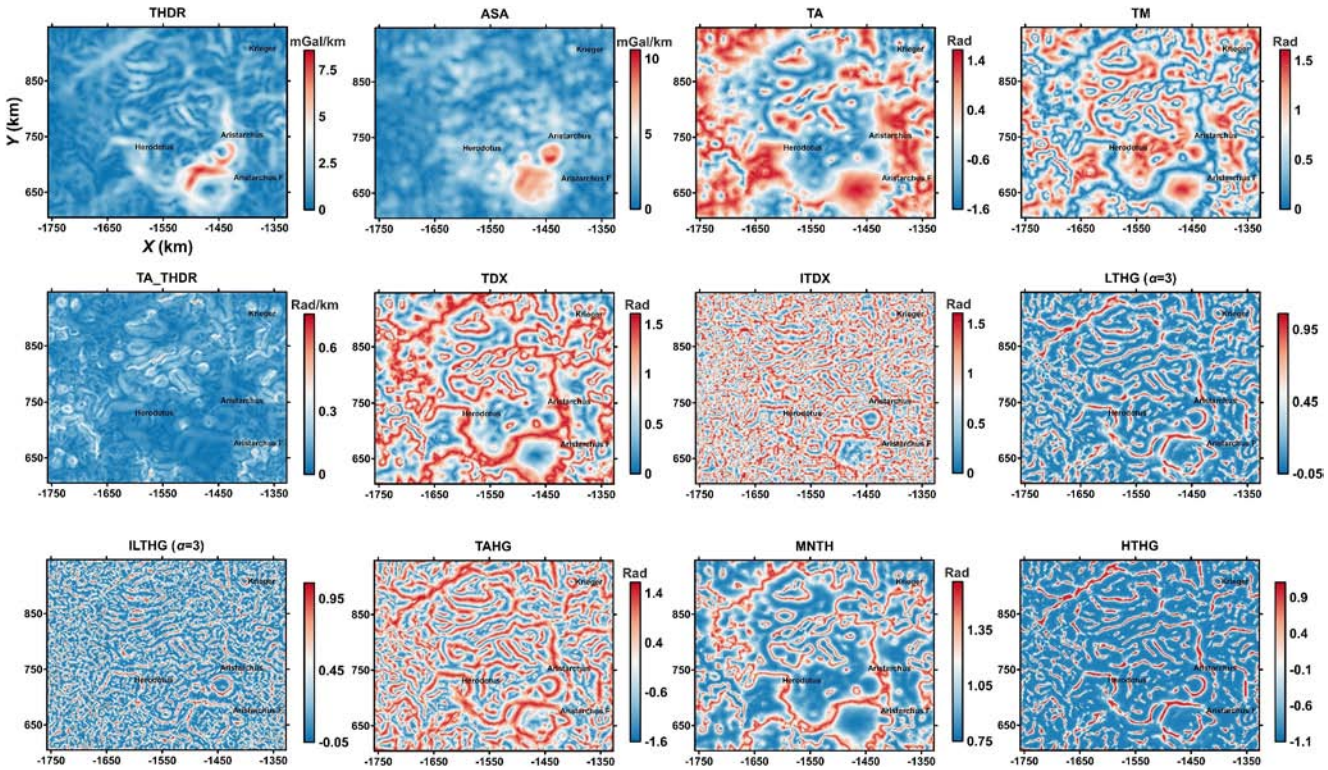

Figure 12. Outputs of the edge detectors directly applied to the lunar gravity anomaly.

works differently compared to the other three methods, as it denoises the data prior to the derivative calculation process. As the results in Figure 16 show, HTHG combined with MNLM yields the best performance, which is consistent with the synthetic tests.

In brief, the experiments with lunar data from the Aristarchus region highlighted the effectiveness of HTHG in edge detection. The noise amplification during derivative calculation can influence the performance of edge detectors; therefore, integrating methods such as MNLM may help produce balanced and clear outcomes. HTHG combined with MNLM proved the best performance in mapping the lateral density contrast variation beneath the study area on the Moon, with the potential to provide more crucial insights into the geological processes shaping the natural satellite.

5. Validation of HTHG Outcomes

To validate the results of HTHG, we applied the mixed-weighted focusing inversion method and the correlation coefficient imaging technique to the extracted profiles shown in Figures 11e and 11f and compared the outcomes from different approaches. Mathematical details of these approaches are given in Appendix E and Appendix F, respectively.

In brief, the derivative-based mixed-weighted focusing inversion method iteratively updates the subsurface density contrast distribution to ensure its computed response matches the observed anomalies. Although this method reconstructs this distribution, its performance can vary considerably based on the selected control parameter values. This sensitivity to parameters is due to the characteristic non-uniqueness of gravity inversion. Therefore, careful parameter tuning is crucial for reconstructing reliable density contrast images. Correlation coefficient imaging, on the contrary, is a fast method that maps subsurface properties without the need for iterative optimization and any parameter tuning. This approach provides only a rough approximate geometry of the causative sources, without calculating the synthetic gravity anomaly. If a grid cell attains a correlation coefficient close to 1, it likely indicates the presence of a causative mass with a positive density contrast. Additionally, a key advantage of this procedure is its independence from model parameters, making it a supportive tool for extracting subsurface information.

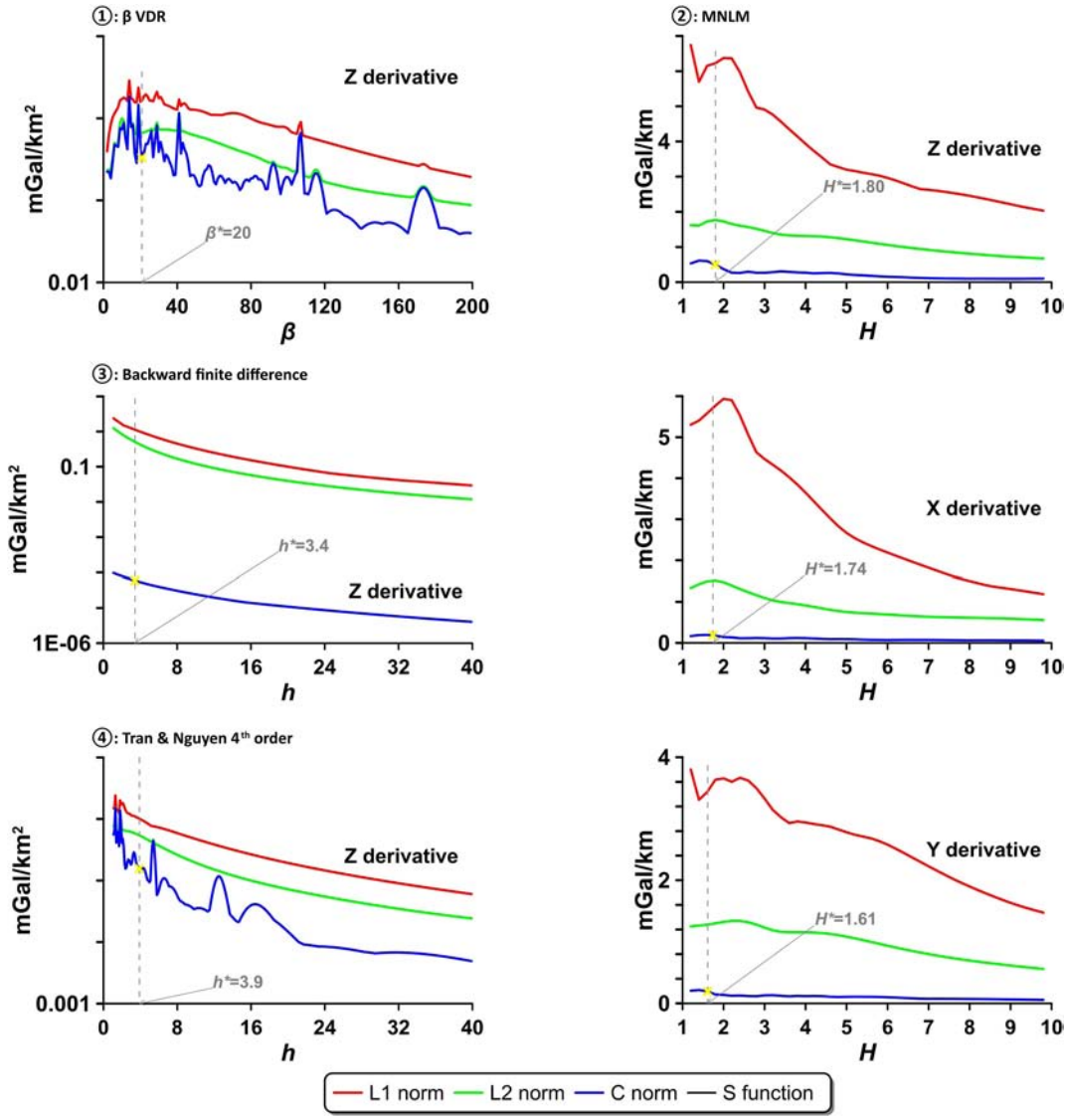

Figure 13. The calculated Lp norms and C norm of the β-VDR, BFD, FTN, and MNLM methods varying with the control parameter coping with the Gravity Recovery and Interior Laboratory data at the Aristarchus plateau. Notably, the calculated Lp norms and C norm related to β-VDR, BFD, and FTN are based on the vertical derivative of Total Horizontal DeRivative. The red, green, and blue curves denote the variation of the values calculated using L1 norm, L2 norm, and C norm.

For the purpose of directly showing the pros and cons of the two inversion strategies, Appendix G gives a synthetic test based on a 2D gravity model. Refer to Appendix G for more details. As the results presented in Appendix G, only by combining more different processing methods (e.g., edge detection, gradient-based inversion, and fast geometric imaging) to cross-validate the obtained results can more reliable interpretation be achieved.

The topographic map along with the HTHG results applied to the denoised data is shown in Figure 17. The map also includes the extracted profiles shown in Figure 11 for direct comparison. Figures 18 and 19 illustrate the HTHG outcomes and density contrast models derived from mixed-weighted focusing inversion and correlation maps for profiles A-A′ and B-B′, respectively. We here used Max_iter = 5, $\mu = 0.1$, $\zeta = 2$, $\xi = 0.8$, and $\varepsilon = 10^{-9}$ to achieve the gradient inversion. Consistent with the synthetic test shown in Appendix G show, the focusing inversion method delivered more refined mapping of density contrast distribution (Figures 18b and 19b), capturing fine-scale subsurface features, whereas the correlation imaging approach produced a smoother

10.1029/2025EA004379

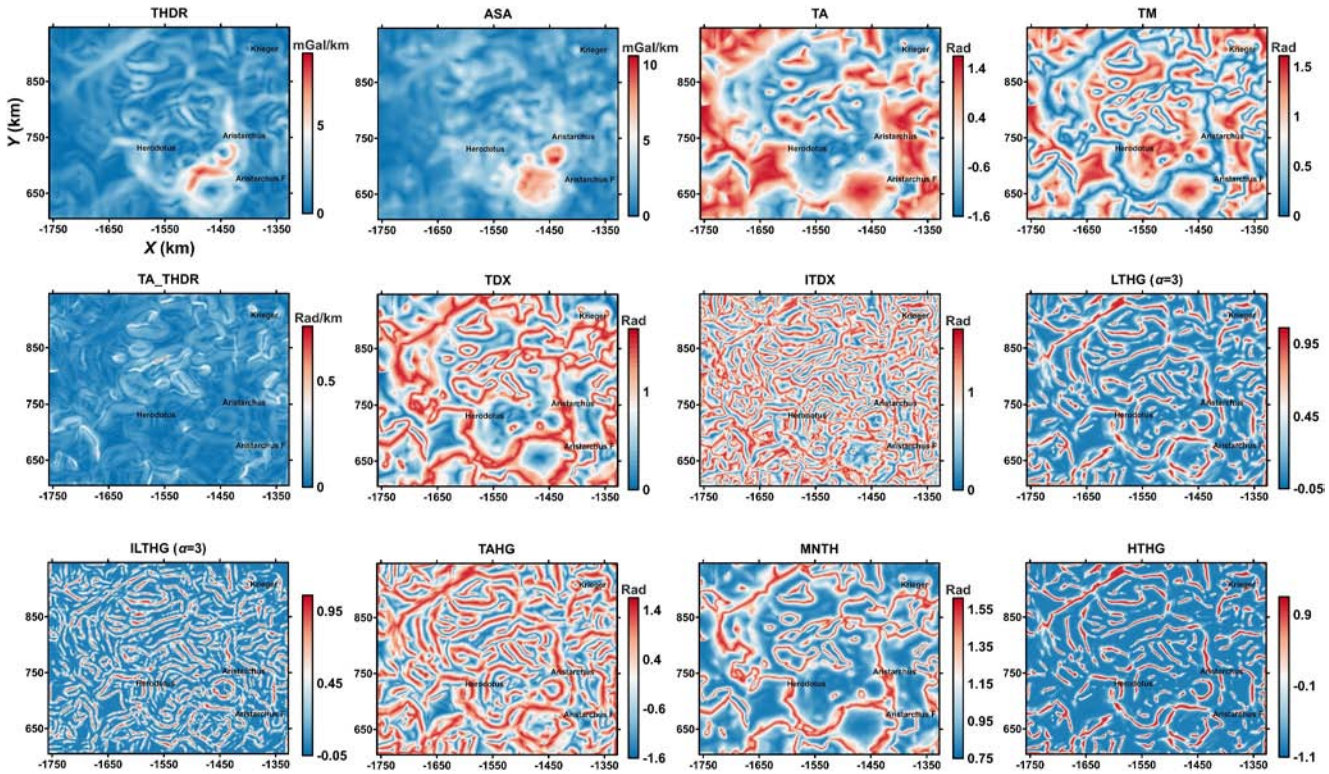

Figure 14. Outputs of the edge detectors applied to the Gravity Recovery and Interior Laboratory data at the Aristarchus plateau denoised using MNLM.

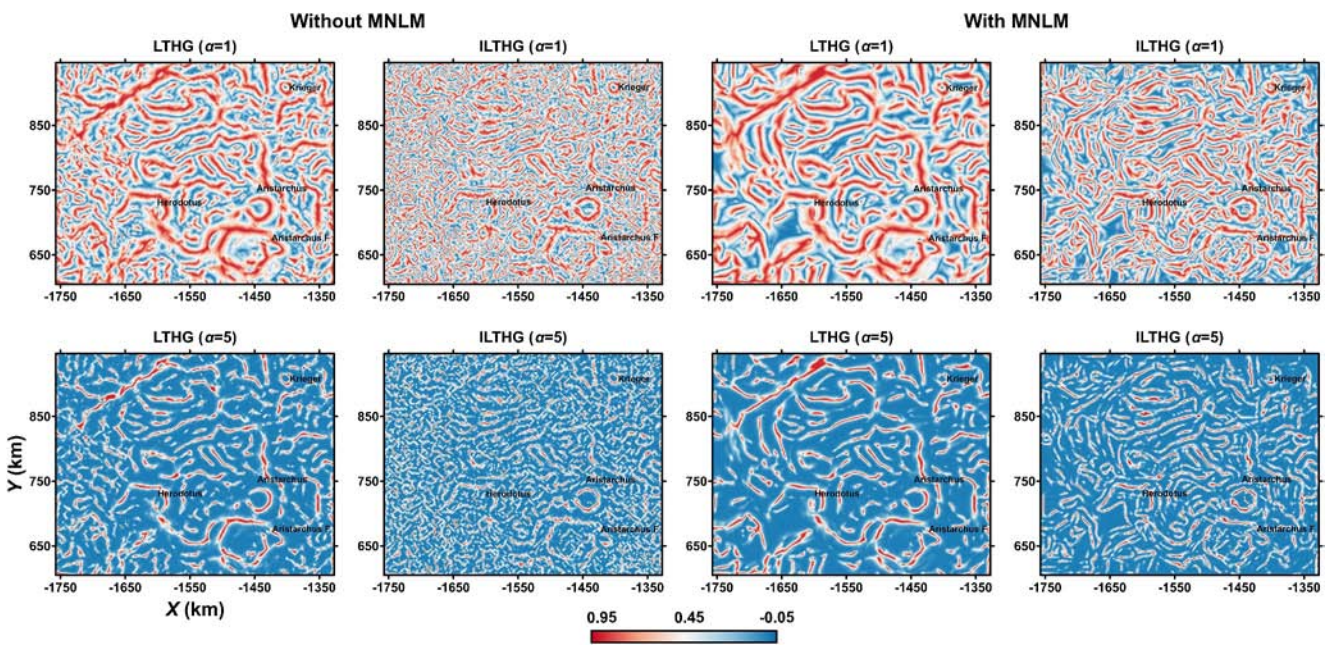

Figure 15. The performance of the LTHG and ILTHG methods with the control parameter $\alpha = 1$ and 5 without (the left two columns) and with (the right two columns) the MNLM method regarding the lunar gravity anomaly at Aristarchus.

10.1029/2025EA004379

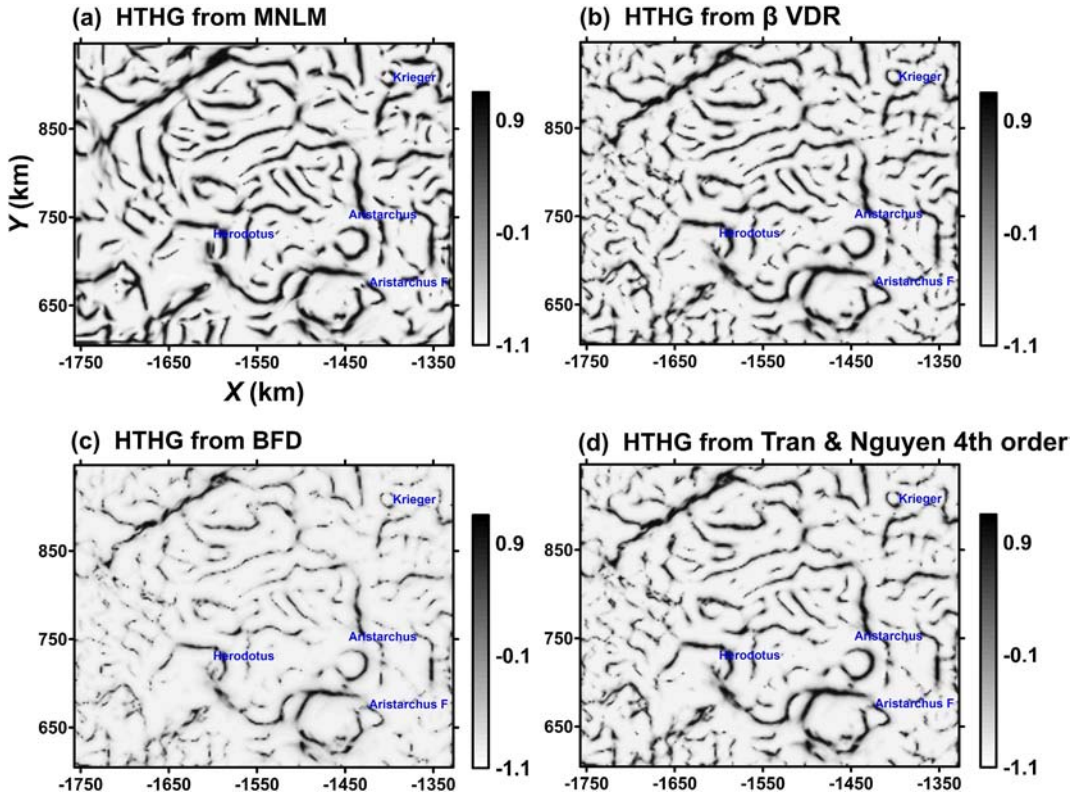

Figure 16. The performance of the HTHG method dealing with the lunar gravity anomaly at Aristarchus with the noise attenuated by MNLM (a), β-VDR (b), BFD (c), and FTN (d), respectively.

structural representation that omits these intricate details (Figures 18c and 19c). Notably, the abrupt lateral changes in density distribution seen in the inverse model satisfactorily mirror the structural boundaries revealed by HTHG, as shown by the dashed lines within Figures 18 and 19. It is clear that the HTHG operator successfully identifies sharp transitions between positive and negative density distributions. The low-density zone from the results of Figures 18 and 19 beneath the Aristarchus crater was distinctly delineated. In Figures 18 and 19, (d) illustrates the data-fitting performance of the focusing inversion method, while (e) and (f) depict the progression of the stopping criteria within three iterations.

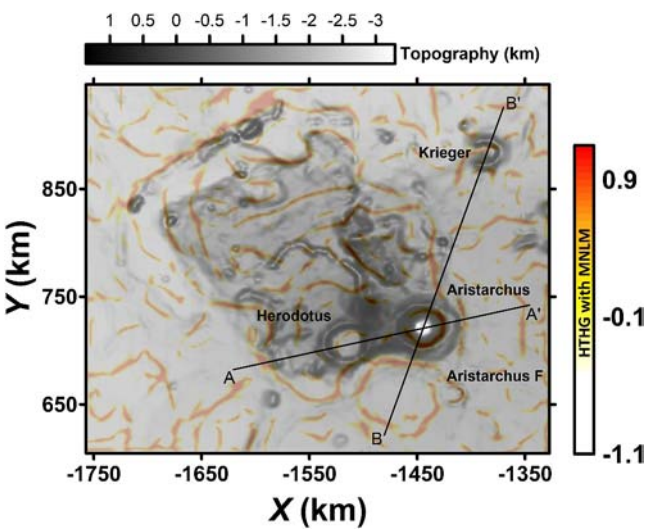

Figure 17. The Aristarchus plateau's topography and HTHG edge-detection results after MNLM denoising. Profiles A-A′ and B-B′ are also displayed.

Furthermore, Figures 20 and 21 demonstrate the density contrast distribution recovered from gravity inversion of the two profiles via the mixed weighting function with three different combinations of control parameters without changing the μ factor (shown in the left column; the exact values of the combinations of control parameters are also denoted within). The associated fitting performance is shown in the right column. For simplicity, the convergence curves are not shown. Each of the recovered density distributions is obtained via the mild alteration of the parameters ζ, ξ, and ε; however, the retrieved models are obviously different. The fitting performance of the three cases is generally the same regarding the lunar data inversion. These features vividly prove the well-known ill-posedness problem of potential field data inversion. Nevertheless, from the general perspective, we can at least know there are bodies buried under the selected profile. We combined the inversion results from different control parameters and the fast correlation

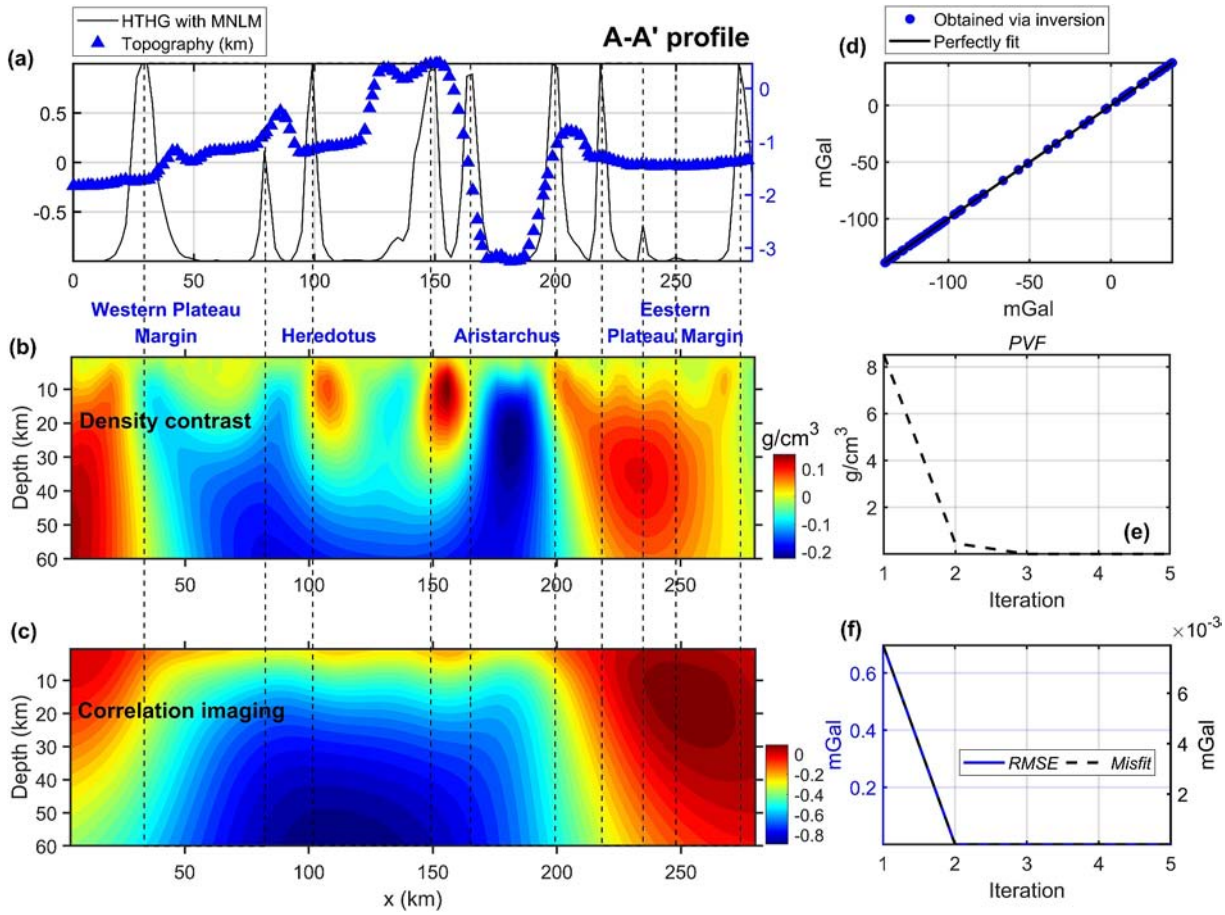

Figure 18. (a) Shows the topography (blue triangles) in kilometers and edge-detection output (solid black line) for the profile A-A′. (b) Shows the density contrast distribution from gravity inversion with a mixed weighting function. (c) Illustrates the estimated subsurface structure using correlation imaging. (d) Shows the successful data fit from the inversion, and (e) and (f) display the stopping criteria variation across iterations, demonstrating convergence within three iterations. Refer to the text for detailed descriptions.

coefficient imaging method and finally determined the algorithm control parameters to be $\mu = 0.1$, $\zeta = 2$, $\xi = 0.8$, and $\varepsilon = 10^{-9}$, used in Figures 18 and 19.

The horizontal range of the low-density zone under the Aristarchus crater is in good agreement with the solution of HTHG. However, HTHG indicated an anomaly zone beneath the Krieger region with two sharp maxima of varying amplitudes, but the gravity inverse model did not produce such a distinct mass distribution in that region due to the possible reasons of data resolution, inversion cell discretization, and inversion uncertainty. The solution map obtained from HTHG efficiently delineated the boundaries between the masses of different densities.

It should be emphasized again that no method is perfect. The derivative-based mixed-weighted focusing inversion can provide the lateral and vertical density distributions with high resolution compared to correlation coefficient imaging, but the results were determined by the algorithm-based control parameters. The correlation coefficient imaging can only provide a rough or ambiguous geometric distribution due to its non-derivative-based implementation, but its results are free from the influence of parameter tuning, even if the measured data is noise-contaminated. The HTHG operator can provide very accurate and high-resolution lateral edge information of the buried structures (unlike the aforementioned LTHG and ILTHG methods, the resolution of HTHG is inherently independent of user-defined parameters); however, it suffers from the small wavelength noise within the obtained data, which will be amplified during the derivative calculation process, so that a noise attenuation method such as MNLM should be integrated with proper tuning parameter selection, making HTHG indirectly parameter-tuning-needed. Therefore, only by integrating the different merits of the edge detection, gradient-based

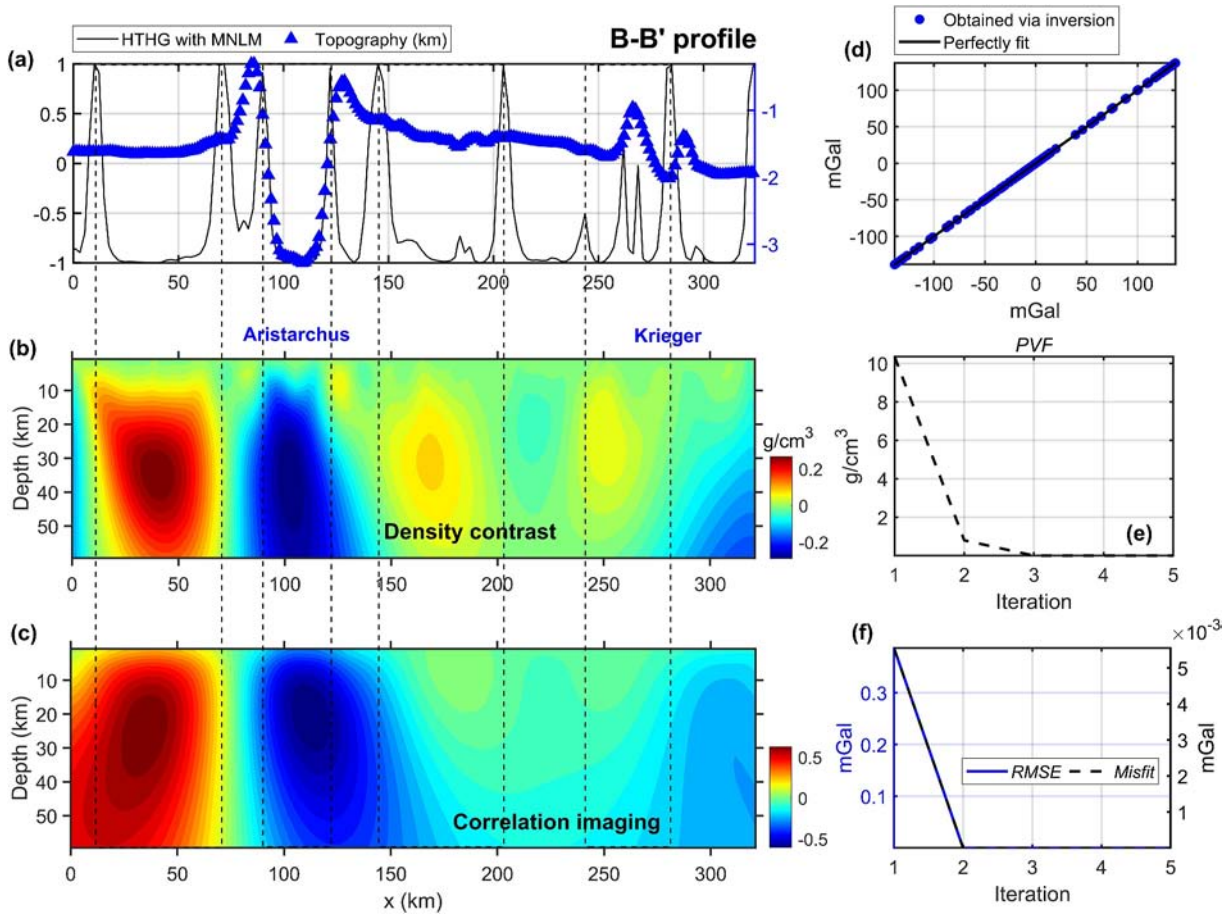

Figure 19. (a) Shows the topography (blue triangles) in kilometers and edge-detection output (solid black line) for the profile B-B′. (b) Shows the density contrast distribution from gravity inversion with a mixed weighting function. (c) Illustrates the estimated subsurface structure using correlation imaging. (d) Shows the successful data fit from the inversion, and (e) and (f) display the stopping criteria variation across iterations, demonstrating convergence within three iterations. Refer to the text for detailed descriptions.

inversion, and fast geometric imaging to cross-validate the obtained results can more reliable interpretation be achieved.

The low-density distribution beneath the Aristarchus crater identified in this study closely aligns with the 3D inversion results reported by Liang et al. (2024). This low-density anomaly is most likely due to the combination of Moho topography, impact-induced fractures, dilatancy, and uplifted material, as detailed by Liang et al. (2024).

6. Conclusions

Edge detection is widely utilized in the interpretation of potential field data for mapping boundaries between geological structures. A wide range of techniques have been developed for delineating the boundaries of geological sources by using different combinations of directional derivatives of potential field anomalies. However, these filtering operators often suffer from artifacts, limited resolution, noise amplification during derivative computations, and challenges in balancing amplitudes of sources placed at different depths. Here, we used the recently proposed HTHG operator, which incorporates the hyperbolic tangent function with horizontal and vertical gradient amplitude derivatives, to overcome these challenges in edge detection procedures. We initially assessed the performance of HTHG in comparison with eleven edge detection techniques using both noise-free and noisy synthetic gravity data sets. In these cases, the HTHG operator showed better performance

10.1029/2025EA004379

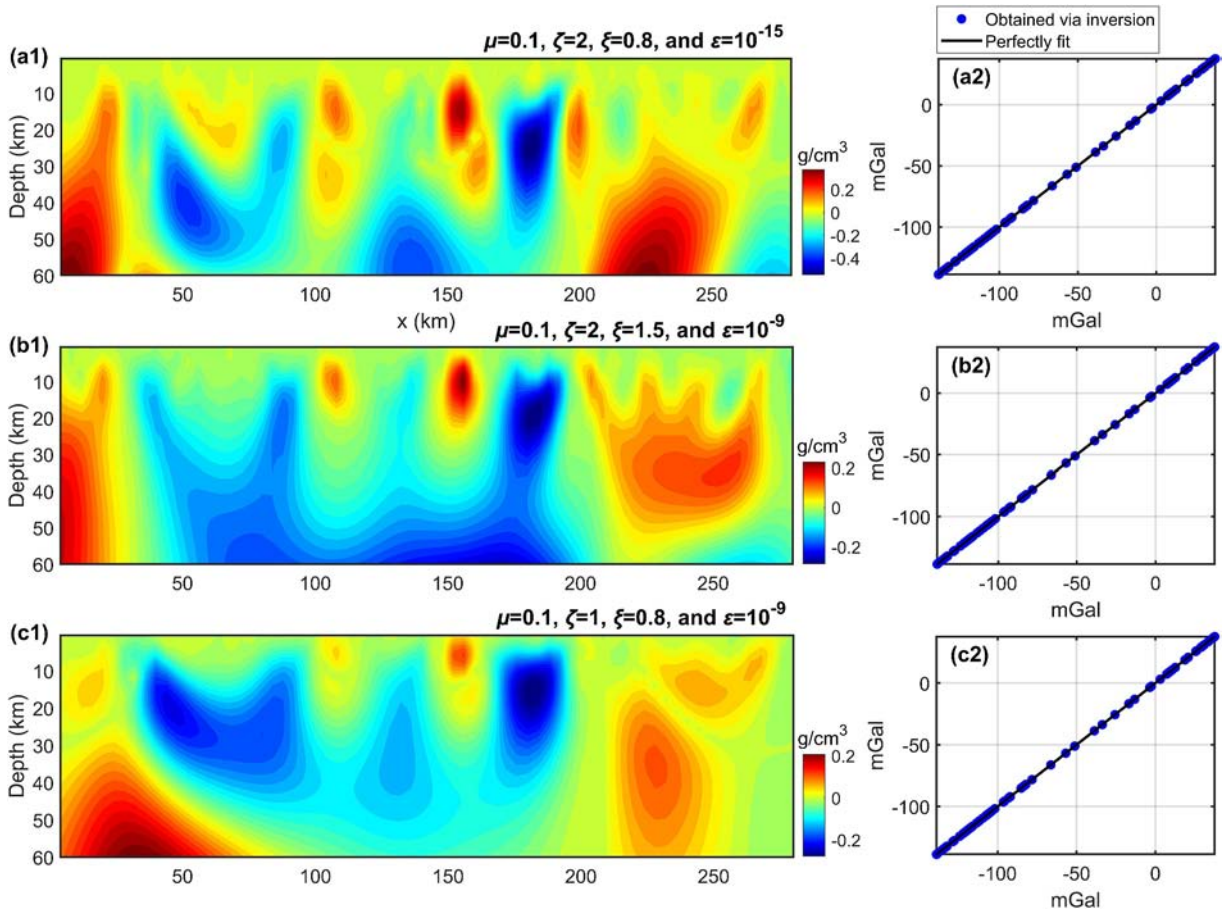

Figure 20. The density contrast distribution recovered from gravity inversion of the profile A-A′ via the mixed weighting function with three different combinations of control parameters without changing the μ factor (shown in the left column; the exact values of the combinations of control parameters are also denoted within). The associated fitting performance is shown in the right column. For simplicity, the convergence curves are not shown.

in delineating source boundaries, achieving higher accuracy, resolution, and amplitude balancing compared to the other detectors in noise-free data case. However, similar to other filters, HTHG exhibited sensitivity to noise amplification during derivative calculations. To address this, we examined various noise reduction techniques and evaluated the effect of parameter tuning for each technique when integrated with the edge detectors. The use of HTHG with MNLM produced the most effective results. Finally, we applied HTHG to the gravity data of the Aristarchus region on the Moon. The results were compared with those obtained from 2D gravity focusing inversion, the correlation imaging algorithm, and the previously reported outcomes of 3D inversion. The findings from edge detection and inversion complemented each other, collectively strengthening the interpretation. The prominent low-density anomalous zone beneath the Aristarchus crater is most likely due to the combined effects of Moho relief, impact-induced fracturing, dilation, and localized uplifted silicic layer. This study highlights the efficacy of the HTHG operator in addressing edge detection challenges and underscore the necessity of integrating various methods, including edge detection, noise suppression, imaging, and inversion, to guarantee the interpretation reliability and enhance our understanding of the Moon's subsurface geological framework.

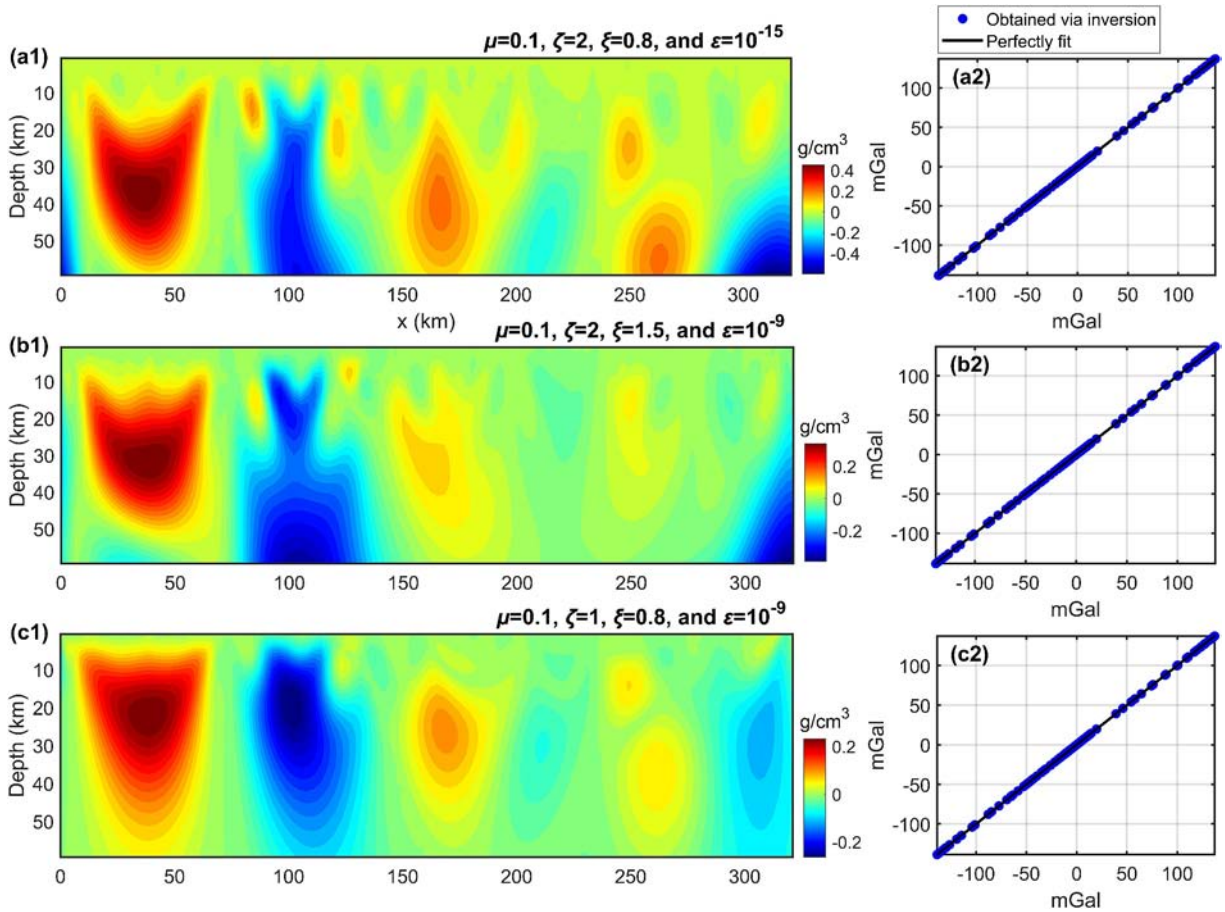

Figure 21. The density contrast distribution recovered from gravity inversion of the profile B-B′ via the mixed weighting function with three different combinations of control parameters without changing the μ factor (shown in the left column; the exact values of the combinations of control parameters are also denoted within). The associated fitting performance is shown in the right column. For simplicity, the convergence curves are not shown.

Appendix A: BFD

The BFD approach is expressed by (Florio et al., 2006):

$$\frac{\partial P}{\partial z} = \frac{\text{P-P}[-(h \times \Delta h)]}{h \times \Delta h} \tag{A1}$$

where the parameter h controls the spacing increment in both horizontal directions.

Appendix B: FTN

Tran and Nguyen (2020) implemented a finite difference approach to enhance the stability of derivative calculations. Here, we used the following definition as recommended by Oliveira and Pham (2022):

$$\frac{\partial P}{\partial z} = \frac{25 \times \text{P-}48 \times P[-(h \times \Delta h)] + 36 \times P[-(2h \times \Delta h)]\text{-}16 \times P[-(3h \times \Delta h)] + 3 \times P[-(4h \times \Delta h)]}{12 \times (h \times \Delta h)} \tag{B1}$$

Similar to BFD, the parameter h controls the FTN approach.

Appendix C: β-VDR Method

The β-VDR technique using a finite difference approach can be used to reduce undesired effects while computing the derivatives (Oliveira and Pham, 2022):

$$\frac{\partial P}{\partial z} = \frac{\sum_{i=1}^{5} c_i P(h_i)}{\Delta h} \tag{C1}$$

where

$$\begin{aligned} c_1 &= \frac{\left(2\beta^3 + 15\beta^2 + 35\beta + 25\right)}{12,} \\ c_2 &= \frac{\left(-8\beta^3 - 54\beta^2 - 104\beta - 48\right)}{12,} \\ c_3 &= \frac{\left(12\beta^3 + 72\beta^2 + 114\beta + 36\right)}{12,} \\ c_4 &= \frac{\left(-8\beta^3 - 42\beta^2 - 56\beta - 16\right)}{12,} \\ c_5 &= \frac{\left(2\beta^3 + 9\beta^2 + 11\beta + 3\right)}{12,} \end{aligned} \tag{C2}$$

where P(h_i) is the upward continued data at $h_i = -\beta\Delta h - (i-1)\Delta h$, Δh is the spacing increment, and β is the stabilizing parameter. In this study, we used Δh = 1/10 of grid spacing.

Appendix D: NLM and MNLM Filters

Buades et al. (2011) introduced NLM as a spatial filter which evaluates the entire data for repeated patterns taking advantage of self-similarities within the data to improve denoising. This filter is expressed by:

$$\tilde{N}(i,j) = \sum_{p=-Ds}^{Ds} \sum_{q=-Ds}^{Ds} \omega(p,q)\, N_{(i,j)}^{\text{searching}}(p,q)/N\_f \tag{D1}$$

where

$$\omega(p,q) = \exp\left(-S(p,q)/H^2\right) \tag{D2}$$

$$N\_f = \sum_{p=-Ds}^{Ds} \sum_{q=-Ds}^{Ds} \omega(p,q) \tag{D3}$$

Here, $N_{(i,j)}^{\text{searching}}$ is a $D \times D$ matrix ($D = 2Ds + 1$) centered at (i, j), ω denotes a weight factor and *N-f* serves as a normalization factor to ensure the weights sum to one, H is proportional to the noise level, while $S(p, q)$ is defined by (Froment, 2014; Wang et al., 2006):

$$S(p,q) = \sum_{a=-ds}^{ds} \sum_{b=-ds}^{ds} G(a,b) \left[N_{(p,q)}^{\text{comparing}}(a,b) - N_{(i,j)}^{\text{comparing}}(a,b) \right]^2 / n\_f \tag{D4}$$

where

$$G(a,b) = \exp\left[-\left(a^2 + b^2\right)/2\sigma^2\right] \tag{D5}$$

$$n\_f = \sum_{a=-ds}^{ds} \sum_{b=-ds}^{ds} G(a,b) \tag{D6}$$

These equations calculate $S(p, q)$ using the weighted Euclidean distance over two matrices of size $d \times d$ ($d = 2\,\mathrm{ds} + 1$). The Gaussian kernel $G(a, b)$ allows for a Gaussian-weighted Euclidean distance in calculations, with the standard deviation σ controlling the kernel spread. Despite the efficiency of NLM, the process can be computationally demanding and highly parameter-sensitive (Manjón et al., 2008; Wang et al., 2006). Addressing these limitations, Ai, Alvandi, et al. (2023) proposed the MNLM filter which combines unweighted Euclidean distance with Integral Image techniques. This modification enhances calculation speed and simplifies parameter tuning. In this study, we used $Ds = 15$ and $ds = 5$, with a focus on the effect of H.

Appendix E: Mixed-Weighted Focusing Inversion

The general formulation for the weighted least-squares inversion is expressed by (Guillen & Menichetti, 1984):

$$\Delta\mathbf{m}^{l} = \left(\mathbf{W}_m^{l-1}\right)^{-1}\mathbf{A}^{T}\left(\mathbf{A}\left(\mathbf{W}_m^{l-1}\right)^{-1}\mathbf{A}^{T} + \mu\mathbf{W}_e^{l-1}\right)^{-1}\Delta\mathbf{d} \tag{E1}$$

$$\mathbf{m}^{l} = \mathbf{m}^{l-1} + \Delta\mathbf{m}^{l}, \Delta\mathbf{d} = \mathbf{d} - \mathbf{A}\mathbf{m}^{l-1} \tag{E2}$$

where $\mathbf{W}$ is the weighting matrix, $\mathbf{A}$ denotes the kernel matrix, $\mathbf{d}$ represents the gravity data, $\mathbf{m}$ is the density contrast vector, l denotes the current iteration, and μ is the damping factor. Ghalehnoee et al. (2016) proposed an effective mixed-weighted matrix which includes compactness ($\mathbf{W}\boldsymbol{c}$) (Last & Kubik, 1983), the depth-weighting ($\mathbf{W}\boldsymbol{z}$) (Li & Oldenburg, 1996, 1998), and the kernel-weighting ($\mathbf{W}\boldsymbol{a}$) (Portniaguine & Zhdanov, 2002). The proposed matrix is given by:

$$\left(\mathbf{W}_m^{l-1}\right)^{-1} = \mathbf{W}_z\mathbf{W}_c^{l-1}\mathbf{W}_a \tag{E3}$$

where

$$\mathbf{W}_z = \begin{bmatrix} z_1^{\zeta} & \cdots & 0 \\ \vdots & \ddots & 0 \\ 0 & 0 & z_{NK}^{\zeta} \end{bmatrix} \tag{E4}$$

$$\mathbf{W}_c^{l-1} = \begin{bmatrix} \left|m_1^{l-1}\right|^{\xi} + \varepsilon & \cdots & 0 \\ \vdots & \ddots & 0 \\ 0 & 0 & \left|m_{NK}^{l-1}\right|^{\xi} + \varepsilon \end{bmatrix} \tag{E5}$$

$$\mathbf{W}_a = \begin{bmatrix} \sum_{i=1}^{N} A_{i1} & \cdots & 0 \\ \vdots & \ddots & 0 \\ 0 & 0 & \sum_{i=1}^{N} A_{iNK} \end{bmatrix} \tag{E6}$$

here, ζ and ξ are the parameters that controls the inversion, and ε is a small value to prevent numerical instabilities. Finally, the data-weighting matrix ($\mathbf{W}\boldsymbol{e}$) is expressed by Ghalehnoee et al. (2016):

$$\left(\mathbf{W}_e^{l-1}\right)^{-1} = \mathrm{diag}\left[\mathbf{A}\left(\mathbf{W}_m^{l-1}\right)^{-1}\mathbf{A}^{T}\right] \tag{E7}$$

The commonly used objective function is the *RMSE* between the simulated and the observed or misfit as given below:

$$\text{Misfit} = \frac{\|\mathbf{d} - \mathbf{d}'\|_2}{\|\mathbf{d}\|_2} \tag{E8}$$

where **d** and **d'** denote the observed and calculated data, respectively. Because of the complex nature of the inversion procedure, the objective functions may not permanently result in efficient iterative performance or produce reasonable outcomes. Hence, we employed the parameter variation function to prevent redundant iterations.

$$\text{PVF} = \left\|\mathbf{m}^{l} - \mathbf{m}^{l-1}\right\|_2 \tag{E9}$$

Appendix F: Correlation Imaging Method

The gravity anomaly f_{cal} caused by a source centered at (x_j, z_k) is defined by:

$$f_{\text{cal}} = \text{G}\Delta\text{M}\frac{z_k}{\left[(x_i - x_j)^2 + z_k{}^2\right]^{3/2}}, i = 1, 2, ..., M \tag{F1}$$

where G is the constant term, ΔM is the mass contrast, and M represents the number of observation points. Accordingly, the derived source imaging function is expressed by (Fedi & Pilkington, 2012; Guo et al., 2009):

$$R(x_j, z_k) = \frac{\sum_{i=1}^{M}\left[f_{\text{obs}}(x_i) - \overline{f_{\text{obs}}}\right] \times \left[\frac{z_k}{\left[(x_i - x_j)^2 + z_k{}^2\right]^{3/2}} - \overline{f_{\text{cal}}}\right]}{\sqrt{\sum_{i=1}^{M}\left[f_{\text{obs}}(x_i) - \overline{f_{\text{obs}}}\right]^2} \times \sqrt{\sum_{i=1}^{M}\left[\frac{z_k}{\left[(x_i - x_j)^2 + z_k{}^2\right]^{3/2}} - \overline{f_{\text{cal}}}\right]^2}}$$
$$j = 1, 2, 3, ..., M;\ k = 1, 2, 3, ..., K \tag{F2}$$

where f_{obs}, $\overline{f_{\text{obs}}}$ and $\overline{f_{\text{cal}}}$ are the observed, mean and calculated anomalies, respectively. M and K represent the number of grid nodes in the horizontal and vertical directions, respectively. The result R is a dimensionless parameter that indicates the likelihood of the source at each grid node (x_j, z_k). When $R(x_j, z_k) = 1$, it suggests a high probability that the grid node (x_j, z_k) contains a body with a positive density contrast.

Appendix G: Synthetic Test for Focusing Inversion and Correlation Imaging

A synthetic 2D gravity model (Figure G1a) was used to mimic the density distribution. The gravity inverse model reconstructed via mixed-weighted focusing inversion is shown in Figure G1b. This reliable outcome was obtained after optimizing the control parameters of the inversion procedure. Through some trial-and-error experiments, we set these parameters as $\mu = 0.1$, $\zeta = 2$, $\xi = 0.8$, and $\varepsilon = 10^{-9}$. In addition, we performed 10 iterations. Figure G1c shows a general and smoother subsurface model produced by correlation imaging. On the other hand, focusing inversion demonstrated better performance by yielding compact, well-defined density distribution that closely conformed to the real model. The data fitting performance and convergence rate of the mixed-weighted focusing inversion using various functions are shown in Figures G1d–G1f.

Notably, Figure G2 illustrates the density contrast distribution recovered from gravity inversion of the synthetic 2D gravity model via the mixed weighting function with three different combinations of control parameters without changing the μ factor (shown in the left column; the exact values of the combinations of control parameters are also denoted within). The associated fitting performance is shown in the right column. For simplicity, the convergence curves are not shown. Each of the recovered density distributions is obtained via the mild alteration of the parameter ζ, ξ, and ε, and the retrieved models are obviously different. The fitting performance of the three cases is also different. These features validate the well-known non-unique problem of gradient-based potential field inversion. Nevertheless, it should be noted that we can at least know there are bodies buried under the selected profile, and the resolution of the recovered model is much higher than that of the correlation imaging method, which does not need any tuning of parameters but can only provide rough geometric information of the causative sources.

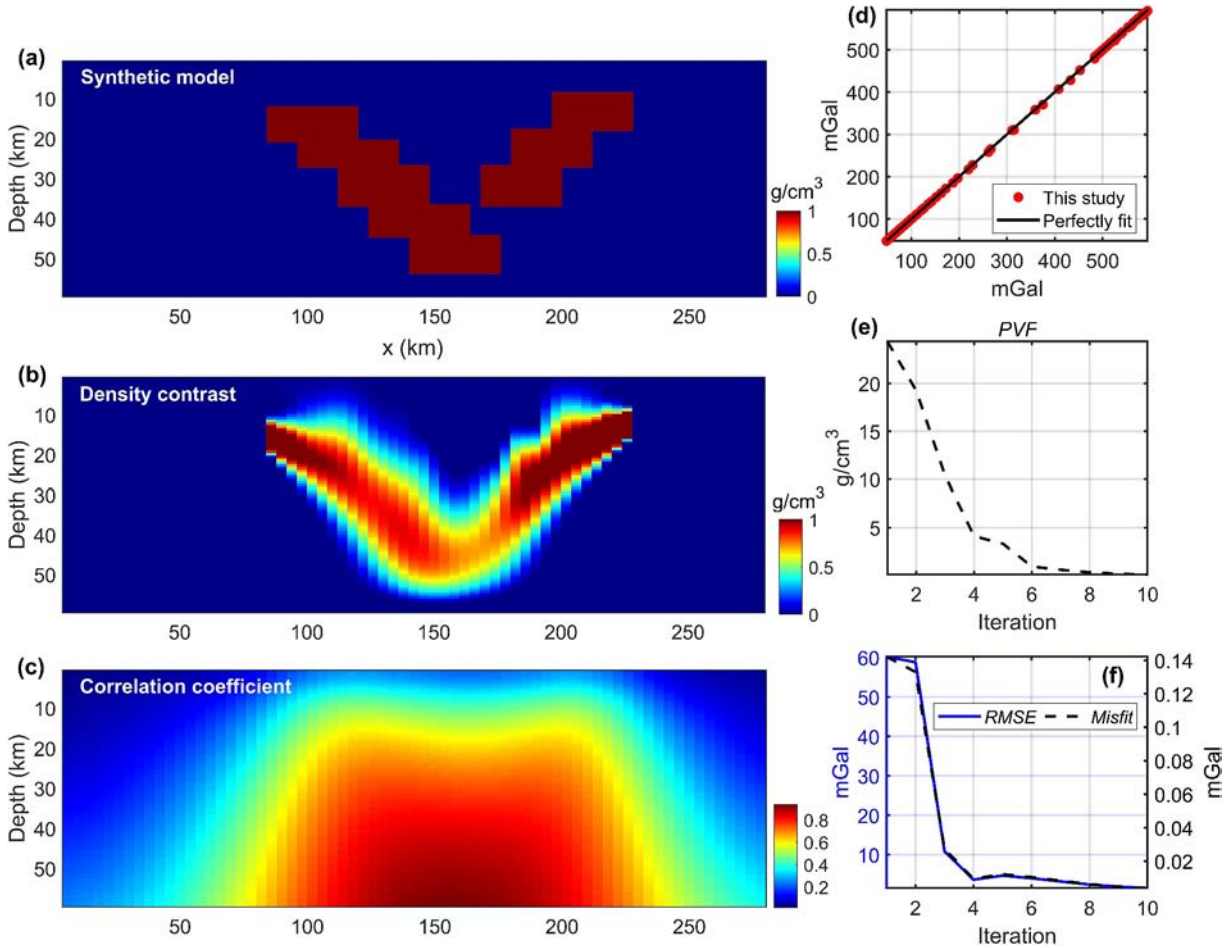

Figure G1. The synthetic 2D gravity model (a), density contrast distribution through focusing inversion (b), estimated subsurface structure using correlation imaging (c), data fitting performance of the inversion (d), and the stopping criteria variation across iterations (e and f).

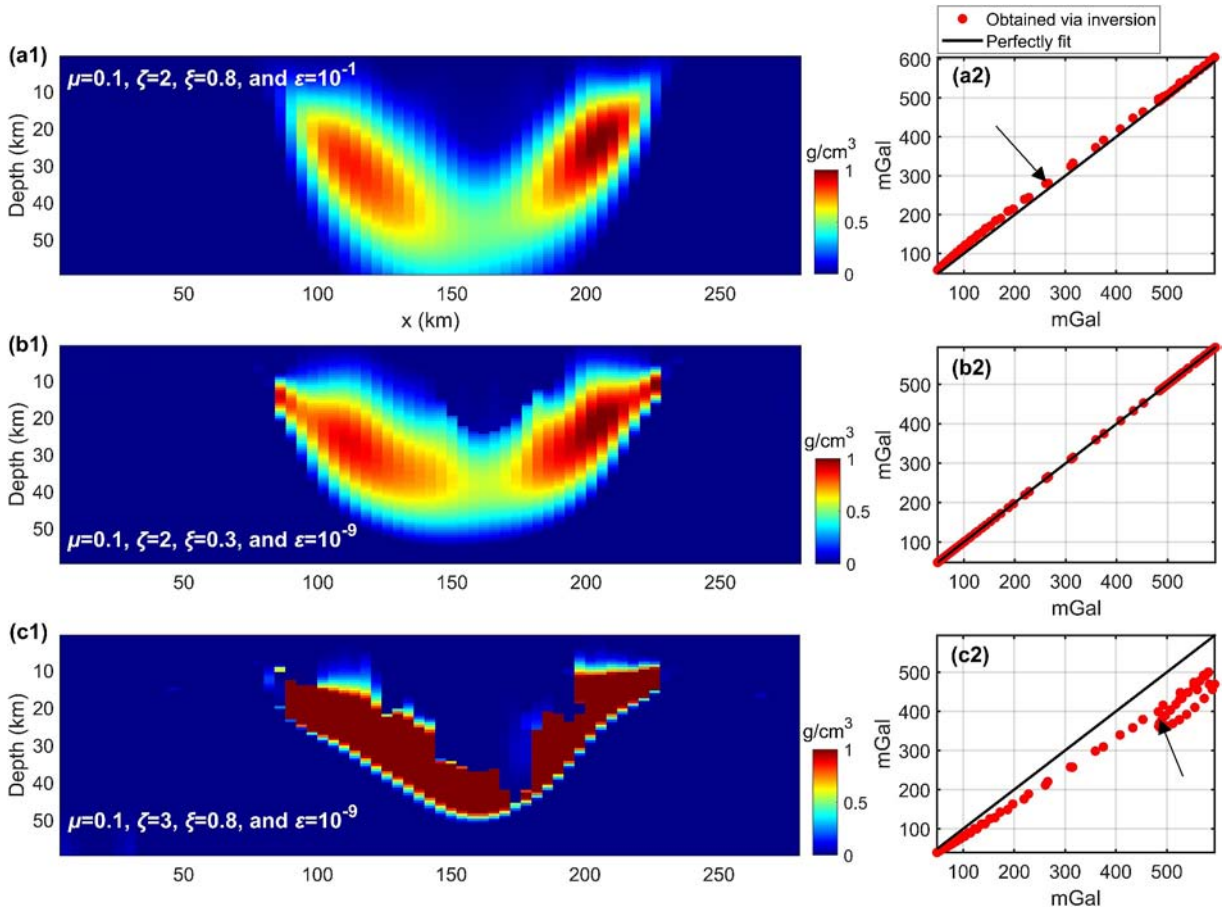

Figure G2. The density contrast distribution recovered from gravity inversion of the synthetic 2D gravity model via the mixed weighting function with three different combinations of control parameters without changing the μ factor (shown in the left column; the exact values of the combinations of control parameters are also denoted within). The associated fitting performance is shown in the right column. For simplicity, the convergence curves are not shown.

Conflict of Interest

The authors declare no conflicts of interest relevant to this study.

Data Availability Statement

Synthetic data sets along with the real data, are detailed in Ai (2025) at https://doi.org/10.5281/zenodo.15104140. The computer code of MNLM is available at the GitHub platform (https://github.com/HanbingAi/Gravity-anomaly-denoising-using-Modified-Non-Local%20Means).

Acknowledgments
This research is funded by the National Key R&D Program of China (2021YFA0715100), the National Natural Science Foundation of China (42030108). We are very grateful to Prof. Roman Pašteka for his constructive comments and suggestions that have improved the quality of the paper.

References

Ai, H. (2025). Data for: Robust edge detection for structural mapping beneath the Aristarchus Plateau on the Moon using gravity data [Dataset]. *Zenodo*. https://doi.org/10.5281/zenodo.15104140

Ai, H., Alvandi, A., Ghanati, R., Pham, L. T., Alarifi, S. S., Nasui, D., & Eldosouky, A. M. (2023). Modified non-local means: A novel denoising approach to process gravity field data. *Open Geosciences*, *15*(1), 20220551. https://doi.org/10.1515/geo-2022-0551

Ai, H., Deniz Toktay, H., Alvandi, A., Pašteka, R., Su, K., & Liu, Q. (2024). Advancing potential field data analysis: The modified horizontal gradient amplitude method (MHGA). *Contributions to Geophysics and Geodesy*, *54*(2), 119–143. https://doi.org/10.31577/congeo.2024.54.2.1

Ai, H., Ekinci, Y. L., Alvandi, A., Deniz Toktay, H., Balkaya, Ç., & Roy, A. (2024). Detecting edges of geologic sources from gravity or magnetic anomalies through a novel algorithm based on hyperbolic tangent function. *Turkish Journal of Earth Sciences*, *33*(6), 684–701. https://doi.org/10.55730/1300-0985.1936

Ai, H., Ekinci, Y. L., Balkaya, Ç., & Essa, K. S. (2023). Inversion of geomagnetic anomalies caused by ore masses using hunger games search algorithm. *Earth and Space Science*, *10*(11), e2023EA003002. https://doi.org/10.1029/2023EA003002

Ai, H., Song, X., Zhang, X., Ekinci, Y. L., Balkaya, Ç., Shekar, B., et al. (2025). Full-parametric and joint inversion of multimode surface wave data for identifying glacial ice thickness and freezing extent in subglacial sediments via the hunger games search algorithm. *Geophysics*, *90*(1), KS1–KS14. https://doi.org/10.1190/geo2023-0756.1

Al-Bahadily, H. A., Al-Rahim, A. M., & Smith, R. S. (2024). Determination of reactivated regions and faults in the Iraq southern desert with the new edge technique, inverse tilt angle of second-gradients (ITAS). *Acta Geophysica*, *72*(3), 1675–1692. https://doi.org/10.1007/s11600-023-01176-4

Alvandi, A., Ardestani, V. E., & Anbaran, S. H. M. (2024). Novel detectors based on the elliott function for mapping potential field data: Application to aeromagnetic data from Indiana, United States. *Annals of Geophysics*, *67*(6), GP656. https://doi.org/10.4401/ag-9146

Alvandi, A., Su, K., Ai, H., Ardestani, V. E., & Lyu, C. (2023). Enhancement of potential field source boundaries using the hyperbolic domain (Gudermannian function). *Minerals*, *13*(10), 1312. https://doi.org/10.3390/min13101312

Barker, M., Mazarico, E., Neumann, G., Zuber, M., Haruyama, J., & Smith, D. (2016). A new lunar digital elevation model from the lunar orbiter laser altimeter and SELENE terrain camera. *Icarus*, *273*, 346–355. https://doi.org/10.1016/j.icarus.2015.07.039

Blakely, R. J. (1995). *Potential theory in gravity and magnetic applications*. Cambridge University Press. https://doi.org/10.1017/CBO9780511549816

Buades, A., Coll, B., & Morel, J.-M. (2011). Non-local means denoising. *Image Processing On Line*, *1*, 208–212. https://doi.org/10.5201/ipol.2011.bcm_nlm

Castro, F. R., Oliveira, S. P., De Souza, J., & Ferreira, F. J. F. (2018). GRAV-MAG SUITE: An open source MATLAB-based program for processing potential field data. In *VIII Simposio Brasileiro de Geofisica. Para, Brazil: Brazilian Geophysical Society*.

Chen, B., Huang, Q., Du, J., Zhang, S., Liu, J., & Xu, C. (2024). The 3-D density structure of the large shield volcanic structure in the Gardner region revealed by a new gravity inversion. *Geophysical Research Letters*, *51*(15), e2024GL108667. https://doi.org/10.1029/2024GL108667

Chevrel, S., Pinet, P., Daydou, Y., Le Mouélic, S., Langevin, Y., Costard, F., & Erard, S. (2009). The Aristarchus Plateau on the Moon: Mineralogical and structural study from integrated Clementine UV–Vis–NIR spectral data. *Icarus*, *199*(1), 9–24. https://doi.org/10.1016/j.icarus.2008.08.005

Cooper, G., & Cowan, D. (2006). Enhancing potential field data using filters based on the local phase. *Computers and Geosciences*, *32*(10), 1585–1591. https://doi.org/10.1016/j.cageo.2006.02.016

Cordell, L. (1979). Gravimetric expression of graben faulting in Santa Fe country and the Espanola Basin, New Mexico, in: Santa Fe Country, Ingersoll. In V. Raymond, L. A. Woodward, & H. L. James (Eds.), *New Mexico geological society, guidebook, 30th field conference* (pp. 59–64). https://doi.org/10.56577/FFC-30.59

Deniz Toktay, H., Ai, H., Alvandi, A., Su, K., & Li, J. (2025). MTAHG and MTBHG: Modified approaches for interpreting gravity data. *Earth and Space Science*, *12*(4), e2024EA003900. https://doi.org/10.1029/2024EA003900

Ekinci, Y. L., Ertekin, C., & Yiğitbaş, E. (2013). On the effectiveness of directional derivative based filters on gravity anomalies for source edge approximation: Synthetic simulations and a case study from the Aegean graben system (western Anatolia, Turkey). *Journal of Geophysics and Engineering*, *10*(3), 035005. https://doi.org/10.1088/1742-2132/10/3/035005

Ekinci, Y. L., & Yiğitbaş, E. (2015). Interpretation of gravity anomalies to delineate some structural features of Biga and Gelibolu peninsulas, and their surroundings (north-west Turkey). *Geodinamica Acta*, *27*(4), 300–319. https://doi.org/10.1080/09853111.2015.1046354

Fedi, M., & Florio, G. (2001). Detection of potential fields source boundaries by enhanced horizontal derivative method. *Geophysical Prospecting*, *49*(1), 40–58. https://doi.org/10.1046/j.1365-2478.2001.00235.x

Fedi, M., & Pilkington, M. (2012). Understanding imaging methods for potential field data. *Geophysics*, *77*(1), G13–G24. https://doi.org/10.1190/geo2011-0078.1

Ferreira, F. J., de Souza, J., de Bongiolo, A. B. e. S., & de Castro, L. G. (2013). Enhancement of the total horizontal gradient of magnetic anomalies using the tilt angle. *Geophysics*, *78*(3), J33–J41. https://doi.org/10.1190/geo2011-0441.1

Florio, G., Fedi, M., & Pasteka, R. (2006). On the application of euler deconvolution to the analytic signal. *Geophysics*, *71*(6), L87–L93. https://doi.org/10.1190/1.2360204

Froment, J. (2014). Parameter-free fast pixelwise non-local means denoising. *Image Processing On Line*, *4*, 300–326. https://doi.org/10.5201/ipol.2014.120

Ghalehnoee, M. H., Ansari, A., & Ghorbani, A. (2016). Improving compact gravity inversion based on new weighting functions. *Geophysical Journal International*, https://doi.org/10.1093/gji/ggw413

Glotch, T. D., Jawin, E. R., Greenhagen, B. T., Cahill, J. T., Lawrence, D. J., Watkins, R. N., et al. (2021). The scientific value of a sustained exploration program at the Aristarchus Plateau. *The Planetary Science Journal*, *2*(4), 136. https://doi.org/10.3847/PSJ/abfec6

Glotch, T. D., Lucey, P. G., Bandfield, J. L., Greenhagen, B. T., Thomas, I. R., Elphic, R. C., et al. (2010). Highly silicic compositions on the Moon. *Science*, *329*(5998), 1510–1513. https://doi.org/10.1126/science.1192148

Goossens, S., Sabaka, T., Wieczorek, M., Neumann, G., Mazarico, E., Lemoine, F., et al. (2020). High-resolution gravity field models from GRAIL data and implications for models of the density structure of the Moon's crust. *Journal of Geophysical Research: Planets*, *125*(2), e2019JE006086. https://doi.org/10.1029/2019JE006086

Guillen, A., & Menichetti, V. (1984). Gravity and magnetic inversion with minimization of a specific functional. *Geophysics*, *49*(8), 1354–1360. https://doi.org/10.1190/1.1441761

Guo, L. H., Meng, X. H., Shi, L., & Li, S. L. (2009). 3-D correlation imaging for gravity and gravity gradiometry data. *Chinese Journal of Geophysics*, *52*, 501–510. https://doi.org/10.1002/cjg2.1370

Hansen, P. C. (1994). Regularization tools: A matlab package for analysis and solution of discrete ill-posed problems. *Numerical Algorithms*, *6*(1), 1–35. https://doi.org/10.1007/BF02149761

Huang, Q., Xiao, Z., & Xiao, L. (2013). Ancient primary crust beneath the Aristarchus Plateau: Constraints from gravity and topography data. *Planetary and Space Science*, *89*, 188–193. https://doi.org/10.1016/j.pss.2013.09.016

Huang, Q., Zhao, J., Wang, X., Wang, T., Zhang, F., Qiao, L., et al. (2020). A large long-lived central-vent volcano in the Gardner region: Implications for the volcanic history of the nearside of the Moon. *Earth and Planetary Science Letters*, *542*, 116301. https://doi.org/10.1016/j.epsl.2020.116301

Ibraheem, I. M., Tezkan, B., Ghazala, H., & Othman, A. A. (2023). A new edge enhancement filter for the interpretation of magnetic field data. *Pure and Applied Geophysics*, *180*(6), 2223–2240. https://doi.org/10.1007/s00024-023-03249-3

Karcol, R., & Pašteka, R. (2025). Regularized derivatives-revisited. *Geophysics*, *90*(3), 1–42. https://doi.org/10.1190/geo2023-0787.1

Kiefer, W. S. (2013). Gravity constraints on the subsurface structure of the Marius Hills: The magmatic plumbing of the largest lunar volcanic dome complex. *Journal of Geophysical Research: Planets*, *118*(4), 733–745. https://doi.org/10.1029/2012JE004111

Konopliv, A. S., Park, R. S., Yuan, D. N., Asmar, S. W., Watkins, M. M., Williams, J. G., et al. (2014). High-resolution lunar gravity fields from the GRAIL primary and extended missions. *Geophysical Research Letters*, *41*(5), 1452–1458. https://doi.org/10.1002/2013GL059066

Kusche, J., & Klees, R. (2002). Regularization of gravity field estimation from satellite gravity gradients. *Journal of Geodesy*, *76*(6–7), 359–368. https://doi.org/10.1007/s00190-002-0257-6

Last, B., & Kubik, K. (1983). Compact gravity inversion. *Geophysics*, *48*(6), 713–721. https://doi.org/10.1190/1.1441501

Li, Y., & Oldenburg, D. W. (1996). 3-D inversion of magnetic data. *Geophysics*, *61*(2), 394–408. https://doi.org/10.1190/1.1443968
Li, Y., & Oldenburg, D. W. (1998). 3-D inversion of gravity data. *Geophysics*, *63*(1), 109–119. https://doi.org/10.1190/1.1444302
Liang, F., Amrouche, M., Yan, J., & Saibi, H. (2024). Detection of subsurface density structures of the Aristarchus Plateau by gravity inversion. *Journal of Geophysical Research: Planets*, *129*(2), e2023JE007856. https://doi.org/10.1029/2023JE007856
Liang, Q., Chen, C., & Li, Y. (2014). 3-D inversion of gravity data in spherical coordinates with application to the GRAIL data. *Journal of Geophysical Research: Planets*, *119*(6), 1359–1373. https://doi.org/10.1002/2014JE004626
Liu, J., Li, S., Jiang, S., Wang, X., & Zhang, J. (2023). Tools for edge detection of gravity data: Comparison and application to tectonic boundary mapping in the Molucca Sea. *Surveys in Geophysics*, *44*(6), 1781–1810. https://doi.org/10.1007/s10712-023-09784-x
Ma, G., Huang, D., & Liu, C. (2016). Step-edge detection filters for the interpretation of potential field data. *Pure and Applied Geophysics*, *173*(3), 795–803. https://doi.org/10.1007/s00024-015-1053-6
Manjón, J. V., Carbonell-Caballero, J., Lull, J. J., García-Martí, G., Martí-Bonmatí, L., & Robles, M. (2008). MRI denoising using non-local means. *Medical Image Analysis*, *12*(4), 514–523. https://doi.org/10.1016/j.media.2008.02.004
Melouah, O., & Pham, L. T. (2021). An improved ILTHG method for edge enhancement of geological structures: Application to gravity data from the Oued Righ valley. *Journal of African Earth Sciences*, *177*, 104162. https://doi.org/10.1016/j.jafrearsci.2021.104162
Miller, H. G., & Singh, V. (1994). Potential field tilt—A new concept for location of potential field sources. *Journal of Applied Geophysics*, *32*(2–3), 213–217. https://doi.org/10.1016/0926-9851(94)90022-1
Mustard, J. F., Pieters, C. M., Isaacson, P. J., Head, J. W., Besse, S., Clark, R. N., et al. (2011). Compositional diversity and geologic insights of the Aristarchus crater from Moon Mineralogy Mapper data. *Journal of Geophysical Research*, *116*, E00G12. https://doi.org/10.1029/2010JE003726
Nabighian, M. N. (1984). Toward a three-dimensional automatic interpretation of potential field data via generalized Hilbert transforms: Fundamental relations. *Geophysics*, *49*(6), 780–786. https://doi.org/10.1190/1.1441706
Oliveira, S. P., & Pham, L. T. (2022). A stable finite difference method based on upward continuation to evaluate vertical derivatives of potential field data. *Pure and Applied Geophysics*, *179*(12), 4555–4566. https://doi.org/10.1007/s00024-022-03164-z
Pašteka, R., Karcol, R., Kušnirák, D., & Mojzeš, A. (2012). REGCONT: A matlab based program for stable downward continuation of geophysical potential fields using Tikhonov regularization. *Computers and Geosciences*, *49*, 278–289. https://doi.org/10.1016/j.cageo.2012.06.010
Pašteka, R., Richter, F. P., Karcol, R., Brazda, K., & Hajach, M. (2009). Regularized derivatives of potential fields and their role in semi-automated interpretation methods. *Geophysical Prospecting*, *57*(4), 507–516. https://doi.org/10.1111/j.1365-2478.2008.00780.x
Pham, L. T. (2023). A novel approach for enhancing potential fields: Application to aeromagnetic data of the Tuangiao, Vietnam. *The European Physical Journal Plus*, *138*(12), 1–11. https://doi.org/10.1140/epjp/s13360-023-04760-1
Pham, L. T., Oksum, E., & Do, T. D. (2019). Edge enhancement of potential field data using the logistic function and the total horizontal gradient. *Acta Geodaetica et Geophysica*, *54*(1), 143–155. https://doi.org/10.1007/s40328-019-00248-6
Pham, L. T., & Oliveira, S. P. (2023). Edge enhancement of magnetic sources using the tilt angle and derivatives of directional analytic signals. *Pure and Applied Geophysics*, *180*(12), 4175–4189. https://doi.org/10.1007/s00024-023-03375-y
Plouff, D. (1976). Gravity and magnetic fields of polygonal prisms and ap-plication to magnetic terrain corrections. *Geophysics*, *41*(4), 727–741. https://doi.org/10.1190/1.1440645
Portniaguine, O., & Zhdanov, M. S. (2002). 3-D magnetic inversion with data compression and image focusing. *Geophysics*, *67*(5), 1532–1541. https://doi.org/10.1190/1.1512749
Prasad, K. D., Pham, L. T., & Singh, A. (2022). Structural mapping of potential field sources using BHG filter. *Geocarto International*, *37*(26), 11253–11280. https://doi.org/10.1080/10106049.2022.2048903
Rao, D. B., Prakash, M. J., & Babu, N. R. (1990). 3D AND 2½ D MODELLING OF GRAVITY ANOMALIES WITH VARIABLE DENSITY CONTRAST1. *Geophysical Prospecting*, *38*(4), 411–422. https://doi.org/10.1111/j.1365-2478.1990.tb01854.x
René, R. M. (1986). Gravity inversion using open, reject, and "shape-of-anomaly" fill criteria. *Geophysics*, *51*(4), 988–994. https://doi.org/10.1190/1.1442157
Saibi, H., Amrouche, M., & Fowler, A.-R. (2019). Deep cavity systems detection in Al-Ain City, UAE, based on gravity surveys inversion. *Journal of Asian Earth Sciences*, *182*, 103937. https://doi.org/10.1016/j.jseaes.2019.103937
Tran, K. V., & Nguyen, T. N. (2020). A novel method for computing the vertical gradients of the potential field: Application to downward continuation. *Geophysical Journal International*, *220*, 1316–1329. https://doi.org/10.1093/gji/ggz524
Verduzco, B., Fairhead, J. D., Green, C. M., & MacKenzie, C. (2004). New insights into magnetic derivatives for structural mapping. *The Leading Edge*, *23*(2), 116–119. https://doi.org/10.1190/1.1651454
Wahba, G. (1990). *Spline models for observational data* (Vol. 59, p. 181). SIAM.
Wang, J., Guo, Y., Ying, Y., Liu, Y., & Peng, Q. (2006). Fast non-local algorithm for image denoising. In *2006 international conference on image processing* (pp. 1429–1432IEEE). https://doi.org/10.1109/icip.2006.312698
Wijns, C., Perez, C., & Kowalczyk, P. (2005). Theta map: Edge detection in magnetic data. *Geophysics*, *70*(4), L39–L43. https://doi.org/10.1190/1.1988184
Ye, Z., Liang, X., Liu, L., Liu, J., Bian, S., Geng, J., & Li, Z. (2024). Boundaries identification of geological structure in lunar Oceanus Procellarum region using full gravity gradient tensor methodology. *Advances in Space Research*, *74*(8), 4146–4159. https://doi.org/10.1016/j.asr.2024.06.081
Yin, H., Huang, Q., Zhang, F., Geng, M., Chen, Y., & Zhao, J. (2024). Magmatic evolution of the Marius Hills, Rümker Hills, and Gardner volcanic complexes on the Moon: Constraints from topography and gravity. *Journal of Geophysical Research: Planets*, *129*(12), e2024JE008421. https://doi.org/10.1029/2024JE008421
Zhao, G., Liu, J., Chen, B., Kaban, M. K., & Du, J. (2021). 3-D density structure of the lunar mascon basins revealed by a high-efficient gravity inversion of the GRAIL data. *Journal of Geophysical Research: Planets*, *126*(5), e2021JE006841. https://doi.org/10.1029/2021JE006841
Zisk, S., Hodges, C., Moore, H., Shorthill, R., Thompson, T., Whitaker, E., & Wilhelms, D. (1977). The Aristarchus-Harbinger region of the Moon: Surface geology and history from recent remote-sensing observations. *The Moon*, *17*(1), 59–99. https://doi.org/10.1007/BF00566853
Zuber, M. T., Smith, D. E., Watkins, M. M., Asmar, S. W., Konopliv, A. S., Lemoine, F. G., et al. (2013). Gravity field of the Moon from the Gravity recovery and interior laboratory (GRAIL) mission. *Science*, *339*(6120), 668–671. https://doi.org/10.1126/science.1231507